A multi-method, multi-scale theoretical study of He and Ne diffusion in zircon

Cécile Gautheron, Duval Mbongo Djimbi, Jérôme Roques, Hilal Balout, Richard Ketcham, Eric Simoni, Raphaël Pik, Anne-Magali Seydoux-Guillaume, Laurent Tassan-Got

A multi-method, multi-scale theoretical study of He and Ne diffusion in zircon

Cécile Gautheron[1]*, Duval Mbongo Djimbi[2], Jérôme Roques[2], Hilal Balout[1, 2], Richard A. Ketcham[3], Eric Simoni[2], Raphael Pik[4], Anne-Magali Seydoux-Guillaume[5,6], Laurent Tassan-Got[2]

1- GEOPS, CNRS, Univ. Paris-Sud, Université Paris-Saclay, Rue du Belvédère, Bât. 504, F-91405 Orsay, France

2- Institut de Physique Nucléaire d'Orsay, CNRS-IN2P3, Univ. Paris-Sud, Université Paris-Saclay, 91406 Orsay cedex, France

3- Jackson School of Geosciences, The University of Texas at Austin, Austin, Texas, U.S.A.

4- CRPG, 15 rue ND des pauvres BP20, 54501 Vandoeuvre-Lès-Nancy Cedex, France

5- Université Clermont Auvergne, CNRS, IRD, OPGC, Laboratoire Magmas et Volcans, F-63000 Clermont-Ferrand, France

6- Univ Lyon, UJM-Saint-Etienne, UCA, CNRS, IRD, LMV UMR 6524, F-42023 Saint-Etienne, France

* corresponding author, cecile.gautheron@u-psud.fr

10 figures; 4 Tables

2 appendices

Abstract

The quantification of He and Ne diffusion behavior in crystals rich in U and Th such as zircon is key for the interpretation of (U-Th)/ ^{4}He and (U-Th)/^{21}Ne thermochronometric ages. Multiple parameters such as chemical substitution, channel obstruction and damage can modify the diffusivity compared to a pristine structure. To investigate the impact of these parameters, we have conducted a theoretical diffusion study combining a series of methods and approaches to address the problem across the necessary range of scales (atomic to crystal size). First, using quantum calculation, we determine the different He and Ne insertion sites, insertion energies and diffusion pathways at the atomic scale for an ideal pristine zircon structure (i.e. damage free). These results serve as input for a 3D random walk simulation of atomic trajectories that provides diffusion coefficients for damage-free zircon crystals. Second, as natural zircon crystals are not perfect, we model the impact of different types of damage and diffusion pathway obstruction at the atomic level on He and Ne diffusion in 3D. The calculated He and Ne diffusion coefficients for pure $ZrSiO_4$ exhibit strongly anisotropic behavior and very high diffusivity along the *c*-axis, and with 3D, closure temperatures of -197°C and -202 °C respectively. The results for He are comparable to previous DFT studies but strongly different from experimental diffusion results; results for Ne are similar in this respect. Modelling the impact of different types of damage (vacancies, recoil, fission, voids or fluid inclusions) and obstruction on He and Ne diffusion reveals important implications for the (U-Th)/He and (U-Th)/Ne thermochronometers. First, obstruction alone does not significantly modify He and Ne diffusion except to reduce anisotropy. Second, trapping is the primary mechanism altering He and Ne diffusion even at low dose, and we predict the maximal trapping energies for He and Ne to be 164 and 320 kJ/mol, similar to values inferred from experimental data. We also propose that the closure temperature increases non-linearly with damage, with effective trapping energy increasing with dose until a threshold, possibly corresponding to a percolation

transition, after which retentivity decreases. Based on field data sets we also anticipate a value for this threshold of around ~2-5×10^{17} α/g, lower than previously proposed. We show Ne to be highly blocked by damage and predict similar diffusion behavior to He, but with higher retentivity. We demonstrate the importance of investigating rare gas diffusion at the atomic level for comparison with experimental data, in order to build a predictive diffusion law at different scales.

1. Introduction

In the last two decades, radiogenic ^{4}He and nucleogenic ^{21}Ne have been used for (U-Th)/^{4}He and (U-Th)/^{21}Ne thermochronology in different minerals such as apatite, zircon and iron oxides for a broad range of geological applications (e.g. Farley and Flowers, 2012; Farley and Stockli, 2002; Gautheron et al., 2006; Reiners et al., 2002; Shuster et al., 2005; Zeitler et al., 1987). Robust He and Ne age interpretation strongly depends on quantitative knowledge of diffusion behavior in crystals, which is linked to the closure temperature Tc (Dodson, 1973), representing to first order the temperature below which He and Ne are significantly retained during cooling. He and Ne diffusion in crystals theoretically follows a simple Arrhenius law with isotropic or anisotropic diffusion. However, it has been shown that, for apatite and zircon, diffusion behavior is highly variable. Experimental data sets have Tc values ranging from 40 to 120°C for He in apatite (Shuster et al., 2006) and from -60 to 190°C for zircon (Guenthner et al., 2013, and references therein). For Ne diffusion in zircon, data are sparse due to analytical difficulties, and Tc estimates come only from indirect assessment and one published abstract (Gautheron et al., 2006; van Soest et al., 2013).

Radiation damage is considered to be a primary contributor to this variability, although the impacts of damage type (alpha, recoil and fission damage) and topology (Frenkel-pair, large damage and amorphous zone) on He diffusion in zircon are not well defined. In addition to forming traps for diffusing elements (Farley, 2000), damage can also change diffusive behavior

for even low-damage zircon by reducing the strong anisotropy along the *c*-axis (Bengtson et al., 2012; Farley, 2007). Similar complications may arise from other imperfections such as inclusions, voids, and defects (Zeitler et al., 2017; Danišík et al., 2017).

The relationship between He diffusivity and dose in zircon suggests another topological effect. Diffusivity has been shown to decrease with increasing dose until a threshold is reached, after which it strongly increases with further damage (Guenthner et al., 2013), although recent work suggests that this threshold dose may vary (Anderson et al., 2017). This flip in behavior may be linked to the onset of percolation, in which overlapping damage zones start to form an interconnected network (Salje et al., 1999), essentially dividing the crystal into two transport regimes, one through normal crystal (albeit with imperfections) and one through the damage network (Ketcham et al., 2013). Superimposed on the complexity of diffusion is the process of annealing, which changes the landscape in which diffusion occurs, as it is happening. Recent work suggests that damage annealing in zircon also may depend on dose (Ginster et al., 2019), further highlighting the challenges to understanding the regime in which diffusion operates.

As a result of this complexity, there are limits to how much progress can be made using exclusively empirical observations and experiments on incompletely-understood natural materials (e.g., Reiners et al., 2004; Reiners, 2005; Cherniak et al., 2009; Guenthner et al., 2013; Anderson et al., 2017; Ginster et al., 2019; Zeitler et al., 2017; Danišík et al., 2017). A rigorous physical understanding of the diffusion process and how it is affected by imperfections is an indispensible complement for the varied and extensive data gathering currently underway. Although the inevitably chaotic and variable nature of damage zones makes them hard to characterize, transport of He and Ne in the areas between damage zones, and between damaged and undamaged crystal, is accessible through theoretical and computational approaches.

Several studies have been conducted using Density Functional Theory (DFT) calculations to quantify the He diffusion coefficient in damage-free zircon (Reich et al., 2007;

Saadoune and De Leeuw, 2009; Saadoune et al., 2009). Independent studies consistently find that He is not expected to be retained in the zircon structure at Earth-surface temperatures; for example, Bengtson et al. (2012) calculate T_c ~ -150°C along the crystallographic *c*-axis. However, recent DFT studies on He and Ne diffusion in apatite and hematite give results more similar to experimental data on real specimens, supporting the veracity and applicability of this theoretical approach (Balout et al., 2017a; Djimbi et al., 2015; Gerin et al., 2017).

In this contribution, we investigate He and Ne diffusion in zircon from atomic to grain scales using a coordinated series of methodologies developed in recent studies (Djimbi et al., 2015, Balout et al., 2017a, b; Gerin et al., 2017) to examine important factors that can modify diffusion rates, including trapping, anisotropy, and path obstruction. As no published Ne diffusion data exist, we use DFT at the atomic scale to build and optimize the ideal zircon unit cell accounting for quantum features, and we inventory the insertion and interstitial sites. Once these sites are identified, we combine the DFT approach with the Nudged Elastic Band (NEB) method to determine the migration energies between them. We complete our atomic-scale characterization using Transition State Theory (TST) to compute jump rates between sites. To extend to a larger scale spanning defects, DFT and TST outputs are used in a Kinetic Monte Carlo (KMC) simulation to determine the diffusion trajectories and the effective diffusion coefficients in 3D. We then compare our results with published experimental data and investigate the processes that can modify He and Ne diffusion in zircon. We simulate and evaluate different hypotheses, such as trapping of He and Ne in damage, and diffusion pathway obstruction, in 3D, and their impact on closure temperature. Finally, we discuss the model implications for the (U-Th)/He and (U-Th)/Ne thermochronometers.

2. Methods, the multi-scale approach

We first provide a general summary of our methods and how they interact with each other, as illustrated in Figure 1. Density Functional Theory (DFT) is a computational modeling

method to calculate the energy of interacting atoms by calculating their external electronic configuration. This is done by solving the Schrödinger equation for the electrons using functionals of the electron density. The DFT just solves static problems, atoms at given positions, and does not include dynamics, contrary to molecular dynamics. However, in contrast to molecular dynamics it includes the quantum effects for the electrons, thereby providing the most accurate energy estimation of an ensemble of interacting atoms. Due to the high calculation time, requiring cluster computing, the number of considered atoms remains small (<150 atoms) compared to a real crystal, and therefore a super-cell containing a small number of motionless atoms is used and an infinite repetition of this super-cell is assumed to represent an infinite lattice. The stable position of the atoms for a crystal lattice is found by nudging atom positions until the total energy is minimized. In the same way, an insertion site for He or Ne is found by inserting it into a pre-computed lattice and finding the positions with the minimum energy with respect to displacement after relaxation of the neighboring atoms.

He and Ne atoms can statistically jump between insertion sites when they vibrate as a consequence of the finite temperature. This is a dynamical process, beyond the scope of DFT, which addresses static configurations only. Therefore, another approach has to be followed, namely the Transition State Theory (TST), which computes the jumps statistically. It is based on a full mapping of the energy field encountered when the inserted atom moves along its path to its neighboring site, as delivered by the DFT analysis. This approach is valid because the Born-Oppenheimer approximation allows consideration of the motion of atoms as quasi-stationary from the electron viewpoint.

The ideal pristine crystal represented by DFT and TST does not capture all the properties of a natural one, which will always contain defects, distortions, dislocations and substitutions, and typically mineral and/or fluid inclusions. However, even in a highly degraded crystal, diffusion occurs in pristine lattice for at least some length scale. The approach we

develop here is to consider the ideal case and see how it should be amended when alterations of the pristine lattice are added. Only when significant amorphisation takes place does this approach become invalid. The alteration of the ideal lattice by vacancies, interstitial atoms, and substitutions breaks the periodicity of the lattice and introduces heterogeneity over length scales much larger than the lattice cell dimension. Their effects on diffusion depend on their energy and their topology. Therefore, the easiest way to study them is the simulation of diffusion by random walk over many lattice cells spanning many defects. For this we use the Kinetic Monte Carlo method (KMC), which operates at the mesoscopic level and delivers diffusion coefficients for a heterogeneous medium, based on the energetics of the DFT and the transition rates of the TST (Figure 1). Finally, to compute He and Ne ages in crystals the diffusion equation has to be solved at the macroscopic level using the diffusivities delivered by KMC, or directly by DFT and TST in case of an ideal crystal.

In summary, DFT calculates the mapping of energy as a function of atom location. TST then computes the transition rates by using this mapping and by making use of thermodynamic equilibrium in phase space. KMC then quantifies the effect of randomly distributed alterations of the crystal-like traps or obstructions, independently of the mechanism producing them (interstitial atoms, substitutions, etc.). This pipeline delivers bulk diffusion coefficients for solving the 3D diffusion equation for a finite grain, as illustrated in Figure 1.

2.1 Density Functional Theory

Following the approach described in detail by Djimbi et al. (2015), we use the Periodic Density Functional Theory (DFT; Hohenberg and Kohn, 1964; Kohn and Sham, 1965), as implemented in the Vienna Ab-initio Simulation Package (VASP) (Kresse and Furthmüller, 1996; Kresse and Hafner, 1993), for all structural optimization and insertion site investigations of both He- and Ne-doped zircon lattices. All parameters were optimized on the zircon unit cell, and the relaxed unit cell geometrical parameters are in good agreement with experimental

values. To minimize the volume relaxation effect due to the incorporation of Ne and He atoms, and to avoid interactions between He or Ne with neighboring cells, the zircon unit cell was duplicated along each spatial direction, resulting in a 2×2×2 super cell consisting of 192 atoms (Figure 2A and 2B). We determine the insertion energy of He and Ne in each interstitial site by relaxing the structure with the help of the gradient technique at constant volume. The insertion energy is defined as the energy needed to bring the He or Ne from outside the crystal into the interstitial site. It is calculated as:

$$E_{ins} = E_{He+zircon} - (E_{zircon} + E_{He}) \quad \text{(Eq. 1)}$$

where $E_{He+zircon}$, E_{zircon} and E_{He} are respectively the absolute energy of the system with He or Ne in the zircon host lattice, the absolute energy of the host lattice, and the energy of the isolated He or Ne atom.

We use the Nudged Elastic Band (NEB) (Jónsson et al., 1998; Mills et al., 1995) method to determine the migration energy between insertion sites. NEB is an efficient approach to estimating the minimum energy path (MEP) and the migration energy between two interstitial sites (E_{mig}^{ij}), which is defined as the difference in energy from when the atom is at the saddle point to when it is in the insertion site. It is also called the barrier energy. The NEB is a chain-of-states method (Elber and Karplus, 1987; Pratt, 1986) found by constructing a series of system images between states. Adjacent images are linked by a spring force to ensure the continuity of the path, thus mimicking an elastic band. In this study, all NEB calculations are performed with a spring constant of -5 eV/Å^2.

2.2. Transition State Theory

Interstitial diffusion occurs through a random walk of an atom from one site in the crystal lattice to another neighboring free one. The atom needs enough energy to accomplish this motion; as there is an energy barrier to overcome, diffusion is a thermally activated process.

As already mentioned, this dynamical process cannot be directly calculated by DFT, which addresses static configurations. However, as the motion occurs in thermodynamic equilibrium the canonical ensemble is assumed in phase space. This leads to the transition state theory (Vineyard, 1957; Voter, 1986; Wert and Zener, 1949), in which the atomic motion is controlled by the jump probabilities, Γ, which depend exponentially on temperature.

$$\Gamma^{ij} = \nu_0 \, e^{-\frac{E^{ij}_{mig}}{k_B T}} \quad \text{(Eq. 2)}$$

$$\text{With } \nu_0 = \frac{\prod_{i=1}^{3N} \nu_i^{init}}{\prod_{i=1}^{3N-1} \nu_i^{*}} \xrightarrow{\text{Vineyard approx.}} \approx \frac{\prod_{i=1}^{3} \nu_i^{init}}{\prod_{i=1}^{2} \nu_i^{*}} \quad \text{(Eq. 3)}$$

$$\text{And } E^{ij}_{mig} = E^{*} - E^{init} \quad \text{(Eq. 4)}$$

Where ν_0 is the attempt frequency; ν_i^{init} and ν_i^{*} are the normal mode frequencies at, respectively, the initial and transition states; E^{ij}_{mig} represents the migration energies; and *N* is the number of atoms in the system. For a molecule with *N* atoms there are 3*N* degrees of freedom. For a non-linear molecule three degrees of freedom can be assigned to translation of a body as a whole (T_x, T_y, T_z) and three to rotations (R_x, R_y, R_z). The remaining motions of the atoms are displacements of the atoms from their mean positions. These fundamental vibrations are referred to as "normal modes". Thus, a non-linear molecule has 3*N*-6 normal modes. In the insertion location, the energy is minimum, and therefore the energy has an upward curvature for any displacement of the inserted atom. This 3D-curvature can be expressed with three eigenvalues, which translate directly to the three normal frequencies. This translation is exactly the same as for any harmonic oscillator like a pendulum. At the saddle point, the same features apply, but only transverse motion relative to the transition path is involved, and therefore there are two frequencies. According to the Vineyard (1957) approximation, for one atom (He or Ne), the energetics of other atoms are not affected by the position of the migrating atom being considered. The TST allows thus provides a well-understood theoretical approach for calculating the frequency factor (Figure 1).

2.3. Kinetic Monte Carlo Method

In a pristine lattice, the activation energy (E_a) corresponds to the migration energy obtained from DFT, and the frequency factor (D_0) can be extracted directly from the TST formulas (Fig. 1). However, when obstructions occur the diffusivity depends on their topology, and a simulation over macroscopic crystals has to be run to determine the modified diffusion coefficients. The Kinetic Monte Carlo (KMC) method (Bortz et al., 1975; Gillespie, 1976) is particularly apt for our purposes because it can be used to extend simulation to time scales far beyond the vibrational period and lengths much larger than the cell size. The KMC simulates, at a given temperature, a random walk over the interstitial sites based on the microscopic jump probabilities (Γ), which have been calculated from TST using the DFT results (Fig. 1). In addition, it takes into account potential obstructions and traps, as well as anisotropy.

For a selected temperature, one He (or Ne) atom is placed randomly in one available insertion site. For the possible diffusion directions, with the calculated jumping frequencies given by the TST, we randomly choose a number to simulate the jumping time for each direction. The distribution of jumping times follows an exponential decay. The jump direction with the lowest time is chosen, the time and coordinate are updated, and the time is added to the total travel time. This is repeated *m* times for each atom, and *n* trajectories (atoms) are simulated, using the method of Djimbi et al. (2015). For each trajectory, the total time is computed as the sum of the residence times in each site between jumps. The diffusion coefficient is obtained by averaging over the ensemble of *n* trajectories. If $<x^2>$, $<y^2>$, $<z^2>$ are the averages over the trajectories of the squares of distances between initial and final points in *x*, *y* and *z*, $<t>$ is the average time of the trajectories, and if we denote as D_x, D_y, D_z the diffusion coefficient along the axes, then according to the Einstein relation.

$$D_x = \frac{<x^2>}{2<t>}$$

$$D_y = \frac{<y^2>}{2<t>} \quad \text{(Eq. 5)}$$

$$D_z = \frac{<z^2>}{2<t>}$$

From the above relations the diffusion coefficients can be assessed even in the case of anisotropic diffusion, as is necessary for zircon. The temperature dependence is obtained by running the random walk at different temperatures.

To account for highly anisotropic behavior along the *c* axis and its possible obstruction, the random walk operates on a sub-lattice of 128×128×4096 interstitial sites. When an atom jumps against an edge of the sub-lattice it is automatically re-inserted into the opposite side, so that the geometry can be considered as infinite with a periodicity given by the size of the sub-lattice. Obstructions are simulated by inhibiting some fraction of sites randomly distributed over the sub-lattice.

2.4 3D diffusion modeling

Finally, these two descriptions provide a bulk diffusion coefficient, which is used to calculate the diffusion over a finite grain where the surface is taken into account by solving in 3D the diffusion equation appropriate to surface boundary conditions. A modified version of the rare gas 3D diffusion code published in Gautheron and Tassan-Got (2010) and used in subsequent studies (Djimbi et al., 2015; Gautheron et al., 2009; 2012) has been implemented to simulate He and Ne diffusion in zircon. This code solves the diffusion equation by a Monte Carlo method at the macroscopic level, using the diffusivity extracted from the KMC

simulation. This approach accounts for crystal surface boundaries, which is not possible in the KMC code.

3. Results

3.1. Investigation of He and Ne interstitial sites

Zircon crystallizes as a body-centered tetragonal unit cell, with a structure consisting of a chain of alternating edge-sharing (SiO_4) tetrahedral and (ZrO_8) triangular dodecahedra parallel to *c*-axis (Figure 2A and 2B). The lateral connection of these chains provides two types of possible sites (S_1 and S_1') into which He or Ne atoms can be inserted; these insertion site positions, and the diffusion pathways between them, are identical He and Ne. The connection of these interstitial sites provides open channels along each direction in which He or Ne could diffuse (Figure 2A' and 2B'). In this part of our analysis, a periodic–DFT is run first to build an optimized model of zircon. Next, the model is used to identify diffusion channels and all possible interstitial insertion sites for both He and Ne atoms. As mentioned above, a 2×2×2 supercell was optimized as the host lattice (Figure 2), which was large enough to simulate and study the He and Ne insertion in the zircon crystal lattice free of boundary effects.

The *c*-axis channel is formed by alternating edge-sharing SiO_4 tetrahedron and ZrO_8 dodecahedron units (Figure 2A), and Figure 2A' illustrates the different He (or Ne) insertion sites along this pathway. In each *c*-channel four sites are inventoried for each lattice cell and they are energetically identical due to the symmetries of the crystal. They are spaced by 1.5 Å. Two types of sites are recognized: S_1, which allows a jump to an adjacent *c* channel along *a* (jump along *b* forbidden), and S_1', which allows a jump along *b* to an adjacent *c* channel. Along *c*, the sites form a sequence S_1-S_1'-S_1-S_1' … (Figure 2A'). Therefore, along *a*, diffusion pathways connect S_1 sites. The same applies along *b* with the S_1' sites. The channels along the *a*- and *b*-axis are energetically identical and they will be noted *a*/*b*-(axis or channel) for simplicity. To move along the *a*/*b*-axis, He (or Ne) atoms have to pass through a rhombic

(Rhom.) or rectangular (Rect.) gap as shown on Figure 2B'. The former is formed by the intersection of Zr – Zr and O – O diagonals. The latter is formed by the intersection of Si – Si and O – O diagonals, and its area is much larger than the rhombic gap. Each channel consists of an alternating series of the two gap types (Figure 2B'); for example, along *a* the sequence is S1-Rhom.-S1-Rect.-S1-Rhom.-S1-Rect. This configuration makes the *a*/*b*-channels considerably less diffusive than the *c*-axis due to the narrow rhombic gaps.

After channel determination, the two possible interstitial sites, called S_1 and S_1', were optimized. They are structurally symmetrical and energetically equivalent. Only one interstitial site environment exists for He and Ne, an octahedral-like site formed by the six oxygen atoms. The interatomic He – O distances have three different values of 2.02, 2.22 and 2.36 Å. For the Ne insertion case, the Ne atom is located 2.16, 2.30 and 2.42 Å from neighboring oxygen atoms. These larger distances are due to the larger size of the Ne atom, making the relaxation effect important for Ne.

The insertion energies calculated based on equation 1 for He and Ne in the different insertion sites are listed in Table 1. The derived helium insertion energy is 1.46 eV, which is in good agreement with other DFT calculations performed by Saadoune et al. (2009) and for comparison obtained insertion value in hematite is given (Balout et al., 2017a, b). In the case of Ne, the insertion energy of 3.10 eV is almost twice that calculated for He. This is related to the larger atomic radius of Ne, which must repel the neighboring atoms more to enter the interstitial site.

3.2. Migration Energies (E_{mig})

In the *c*-channel, since the inter-site distance $S_1 – S_1$' is about 1.5 Å, only one image is taken between the two sites for the NEB calculation. Figure 3A and 3A' present the migration energies path results along the *c*-channel for He and Ne migration, respectively. The migration energies, reported in Table 2, are 0.24 eV for He (Figure 3A) and 0.22 eV (Figure 3A') for the

Ne atom. According to *a* (*b*)-channel structures, the S_1 (S_1') sites are separated on one side by a rhombic gap and on the other by a rectangular one. Hence, two NEB calculations were performed for He and Ne migration, corresponding to the energy necessary to pass through each gap. For NEB calculation in this channel we start with a linear path composed of a series of 4 images connecting the two S_1 (S_1') sites. After the relaxation process we found that the migration energy between the sites separated by the rectangular gap is equal to 0.66 and 1.53 eV for He and Ne atoms, respectively (Table 2; Figure 3B). For the rhombic gap, we find a migration energy of 2.60 eV for He, but for Ne the NEB calculation indicated that no migration is possible (Figure 3B'). Figure 4 illustrates the sequence of the interstitial sites along *c* and how they are connected to the pathways along *a* and *b*.

The paradoxical result is that along *c* the energy barrier for Ne is lower than for He, even though its radius is larger as already recognized in the insertion energy calculation. This can be understood by noting that the height of the barrier is a difference in energy. For Ne both the energy in the interstitial site and at the top of the barrier are higher in comparison to He, reflecting the atom radius effect, but this does not say anything about the difference. As a conclusion, contrary to the insertion energy, the activation energy is not well controlled by the ionic or atomic radius. This outcome was already evident in Farley (2007).

According to our results, one can say that, at low temperature, in an ideal crystal He and Ne will diffuse mainly along the *c*-channel. However, as temperature increases, there will be competition between the probability of jumping the 0.24 eV barrier and the 0.66 eV barrier in the case of He diffusion. For Ne-diffusion, however, even at high temperature diffusion along the *c*-axis remains strongly favored.

3.3. Ideal lattice results

Using Transition State Theory as presented in section 2, the attempt frequencies ν, which allow determination of relative jump probabilities, were calculated for each jump case.

All calculated jump probabilities are provided in Table 3. From the parameters listed in this table, the diffusion coefficient along the *c*-axis can be derived analytically for a pristine crystal:

$$D_z = \nu . a^2 . \exp\left(-\frac{E_{mig}}{k_B T}\right) \quad \text{(Eq. 6)}$$

with *a*=1.5 Å. In the same way the diffusivity along *a* and *b* for an undamaged crystal and for practical temperatures ($T<10^4$ K) is obtained as:

$$D_{xy} = \frac{\nu . a^2}{4} . \exp\left(-\frac{E_{rect}}{k_B T}\right) \quad \text{(Eq. 7)}$$

with *a*=3.35 Å. The factor 4 accounts for the fact that only one site over four allows a jump in a given direction (Fig. 4), as crossing the rhombic diamond is quasi-forbidden.

We get respectively for He and Ne:

$$D_{z,He} = 1.6 \times 10^{-7} exp\left(-\frac{0.24}{k_B T}\right) m^2/s \quad \text{(Eq. 8)}$$

$$D_{xy,He} = 1.5 \times 10^{-7} exp\left(-\frac{0.66}{k_B T}\right) m^2/s \quad \text{(Eq. 9)}$$

$$D_{z,Ne} = 1.2 \times 10^{-8} exp\left(-\frac{0.22}{k_B T}\right) m^2/s \quad \text{(Eq. 10)}$$

$$D_{xy,Ne} = 1.1 \times 10^{-7} exp\left(-\frac{1.53}{k_B T}\right) m^2/s \quad \text{(Eq. 11)}$$

From these results one can conclude that Ne diffusivity is slightly higher at low temperature than He diffusivity in a perfect zircon host lattice. In addition, the diffusivity is highly anisotropic and diffusion occurs essentially along the *c*-axis. The anisotropy is even stronger in the Ne case due to the high energy barrier when crossing the rectangular gap.

4. Discussion

4.1. He and Ne diffusion in non-damaged zircon structure

4.1.1. Comparison to previous calculations

Helium diffusivity in zircon, calculated by DFT and molecular dynamics, has already been reported (Bengtson et al., 2012; Reich et al., 2007; Saadoune et al., 2009), and for

363 comparison the insertion energy and barriers are listed respectively in Tables 1 and 2. It is
364 interesting to point out that only Bengtson et al. (2012) recognizes the 1.5 Å inter-site distance
365 along the *c*-axis, which results from the crystal symmetries. Reich et al. (2007) and Saadoune
366 et al. (2009) missed this feature although a dip is visible in the energy landscape for the former,
367 indicating that the minimal energy path was not found along the *c*-axis. Concerning the
368 migration energies, which have the strongest impact on the diffusivity, we are in good
369 agreement with Saadoune et al. (2009) along the *c*-axis, and at variance with the other
370 calculations. Although we found the same energy pattern along this channel as Bengtson et al.
371 (2012), our migration energy is lower. As the variations of the energy along this channel are
372 small the computations of the barrier are very sensitive to the finding of the minimum energy
373 path. When comparing to the previous calculations along the *a/b* directions we find the same
374 barrier across the rhombic gaps, but a higher one through the rectangular gap (0.66 instead of
375 ~0.45 eV, Figure 4, Table 2), for a reason which is not elucidated. We will see later that this is
376 barrier is the one that mainly controls the diffusivity in zircon in practical situations.
377 Concerning He diffusivity, differences exist with respect to the other calculations
378 beyond the migration energy. Reich et al. (2007) and Saadoune et al. (2009) used a 1D formula
379 which is known to be inadequate because it assumes that the energetic shape around the
380 interstitial site and the saddle-point is the same. However, this assumption only acts on the pre-
381 exponential factor and its impact is limited. Bengtson et al. (2012) did not use this assumption
382 but assumed that along *a*/*b* the higher barrier (~2.6 eV) dominates, disregarding the relatively
383 easy intermediate jump along *c* that can bypass this barrier. This explains why they obtained a
384 very low diffusivity along *a*/*b*.
385 **4.1.2. Comparison to experimental data**
386 For Ne only one abstract reports diffusion data, with an E_a value of ~339 kJ/mol and
387 closure temperature of 396-410°C for a 10°C/Ma cooling rate (van Soest et al., 2013). This

388 value is much higher than that computed in this work. Similarly, He diffusion data obtained on
389 natural zircon crystals present significantly higher apparent activation energies than obtained
390 by theoretical studies. In addition, measured (U-Th)/He and (U-Th)/Ne zircon ages confirm that
391 He and Ne are strongly retained in this mineral. For illustration, Figure 5 presents some He
392 diffusion data obtained on natural zircon crystals (e.g., Reiners et al., 2004; Cherniak et al.,
393 2009; Guenthner et al., 2013) compared to our data for a pristine zircon. In detail, Figure 5
394 shows the distribution of activation energy, frequency factor and closure temperature for He
395 obtained for natural zircon, and the deduced activation energy for Ne needed to explain a (U-
396 Th)/Ne age (Gautheron et al., 2006). The authors based their estimate on the known thermal
397 history of the Gold Butte, Nevada area (Reiners et al., 2000) and measured ZNe ages (777±122
398 and 963±164 Ma) that are much older than the ZHe age (19.1±1.5 and 16.7±1.3 Ma
399 respectively). From this, they deduced a closure temperature for Ne in zircon of ~400±50°C,
400 similar to the diffusion data from Van Soest et al. (2013). The activation energy for Ne in zircon
401 should thus be greater than the one for He (i.e., >170 kJ/mol), as Ne appears much more strongly
402 retained than He (Figure 5), in contradiction with the result of our calculation in which a larger
403 diffusivity is found along *c*. Based on the linear relationship between E_a and closure
404 temperature, for Ne we can anticipate an activation energy value above ~170 kJ/mol, but we
405 cannot clearly define the upper limit, and the lower limit is below the value determined by van
406 Soest et al. (2013).

407 ### *4.2. Processes modifying He and Ne diffusion*

408 A strong discrepancy exists between results obtained using theoretical and experimental
409 approaches, leading to a misinterpretation of the validity of the theoretical method. However,
410 recent DFT studies on He and Ne diffusion in apatite (Djimbi et al., 2015) and hematite (Balout
411 et al., 2017a; b), which produce expectations consistent with experiments, bring a strong credit
412 to this theoretical approach. If the discrepancy is not due to a methodological issue, additional

features and processes are likely to be modifying He and Ne diffusion in zircon, as already discussed by Reich et al. (2007), Saadoune et al. (2009) and Bengtson et al. (2012).

Until now, our calculation has only considered an ideal pristine crystal, but in real crystals defects are present and change local diffusion properties. The defects can be substitutions in which an atom of the ideal lattice (Zr usually) is exchanged for another, such as a rare earth element. Another type is Frenkel pairs, consisting of an atom knocked out from its original lattice site, leaving a vacancy, and inserted somewhere else. Frenkel pairs are thermally activated and exist at any temperature, meaning that they can be created and recombined by thermal motion. They are highly enhanced by irradiation due to the decay of U and Th. The first effect of the alpha particle, and more strongly, the recoiling daughter is to create Frenkel pairs by knocking atoms out of the lattice. For high radiation doses the density of vacancies and interstitial atoms becomes high enough to make the lattice unstable, collapsing it into amorphized zones. The diffusivity in such zones is not known and only hypotheses can be proposed. Dislocations are yet another likely pervasive defect type that can alter diffusional pathways. The detailed description of these defects is far beyond the scope of this work. Similarly, meso-scale features that may alter diffusivity and retention, such as mineral and fluid inclusions, are also beyond our scope. Our methodology is based on a simple modeling of their effect on the diffusion of inserted He and Ne atoms, by considering that they diffuse in an ideal crystal (Figure 6A) until they find some defect altering the diffusion (Figure 6B and 6C). We address only two phenomena, obstruction and trapping.

Obstruction may occur when an interstitial atom, knocked out due to irradiation for example, is already in an interstitial site, preventing He or Ne from entering the site. This mechanism is efficient for slowing down diffusion along fast pathways along the *c*-axis in zircon, because it requires the atom to jump over higher barriers to span long distances. The motion is illustrated in Figure 6B, whereas Figure 6A shows the ideal case where the jumps

438 occur primarily along the *c*-axis due to the low barrier. Obstruction can also result from
439 chemical substitutions that alter the energetics along the diffusion pathway. This has been
440 shown to occur for Cl-rich apatite compared to F-apatite (Djimbi et al., 2015), although the
441 authors demonstrate that a significant effect on diffusion only occurs at a relatively high
442 substitution level (some dozens of percent of the halogen sites) in that mineral. For zircon, Hf
443 substitution can be quite important (some wt% percent, e.g., Hanchar and van Westrenen, 2007)
444 and will modify He diffusivity. Dislocations could also lead to obstruction by a local shrinking
445 of the original cell. In Figure 6B for example, the He atom first diffuses along the *c*-axis and
446 crosses the rhombic gap but is then blocked due to the obstruction. Finally, the He atom will go
447 back as it will demand too much energy to cross the rectangular gap, where the migration energy
448 is 2.6 eV (251 kJ/mol). As already emphasized in Djimbi et al. (2015), obstruction is very
449 efficient in reducing diffusion anisotropy, which is an important feature in the case of zircon.
450 The other effect we consider is trapping. This phenomenon has been already considered
451 in several works (Farley, 2000; Shuster et al., 2006; Gautheron et al., 2009; Flowers et al., 2009;
452 Shuster and Farley, 2009; Gerin et al., 2017) and can result from different kinds of defects.
453 When vacancies are created, in particular under irradiation, they offer more space to the
454 diffusing atom at lower energy. Therefore additional energy, noted (ΔEa_T), is necessary to
455 extract it from its location and bring it to a normal interstitial site. In general, trapping may
456 occur in any situation where the interstitial atom has more space to be accommodated. The
457 amorphized zones could offer this more open space and serve as He and Ne storage. If the zones
458 are not interconnected, diffusion still occurs through an ideal lattice endowed with trapping
459 volumes. Even substitutions in some cases can act as traps. Saadoune and de Leeuw (2009)
460 demonstrate that when U^{4+} and Pu^{4+} are present at the percent level in the zircon lattice in the
461 vicinity of an He insertion site, U and Pu increase He solubility by decreasing He insertion
462 energy, leading to a trapping effect.

Radiation damage is the favored mechanism producing trapping because it creates vacancies, and in the case of zircon amorphized zones (Figure 6C). This mechanism was initially proposed for apatite, where radiation damage strongly influences He diffusion by trapping He inside damage (Farley, 2000; Shuster et al., 2006). As a guideline, the maximum available trapping energy corresponds to a case where the diffusing atom is far from its neighbors, such as in a cavity (large damage, voids, fluid inclusions). Any short distance to its neighbors will repel it and increase its energy, thereby reducing (ΔEa_T). The extreme case where the atom is far from any other atom is equivalent to an atom outside of the crystal, and in this case the trapping energy is merely the insertion energy. Therefore, the maximal trapping energy is the insertion energy. The only exception to this rule would occur if atoms in the crystal would interact with the He or Ne by attracting it. Gerin et al. (2017) described the energetics of this process for apatite but similar conclusions can be drawn for zircon. As the insertion energy is 1.46 and 3.1 eV for He and Ne respectively, one can infer that the maximal trapping energy for large damage such as recoil damage (ΔEa_T) will be respectively 1.46 eV (with global *Ea* 1.7 eV = 1.46+0.24 eV; 164 kJ/mol) and 3.31 eV (with global *Ea* 3.32 eV = 3.10+0.22 eV; 320 kJ/mol). In crystals with real damage, different geometries of defects are present, entailing a distribution of ΔEa_T. In addition, when radiation damage accumulates vacancies can connect creating larger spaces, increasing the trapping energy. Figure 6C illustrates a diffusion trajectory with different topologies of damage, with small damage (such as point defects), single recoil damage or recoil damage clusters. The ΔEa_T will be different for each case according to the available free space. An important feature of trapping is that, unlike obstruction, it has no effect on the anisotropy of diffusion, so that it cannot be responsible for the reduction of the anisotropy in case of zircon, although it has the capability to reduce diffusivity strongly, and may be spatially associated with other defects.

4.3. Impact of blocking pathways, i.e. obstruction, on He and Ne diffusion in zircon

It is expected that atoms displaced into the *c*-axis channel as a result of radiation damage strongly affects diffusion along *c*, which is quasi-free at normal temperature in an ideal lattice. In this section, we test the obstruction model using the KMC method and discuss the impact of obstructed pathways on He and Ne diffusion coefficients, by using the model described in section 2.3; additional details are given in Appendix A.

Figure 7 presents the dependence of the diffusion coefficient $D_{a,b}$ and D_c (respectively along *a*, *b* and *c*-axis) as a function of inverse temperature for a set of fractions of obstructed sites (1, 5, 10, 20%). We define the obstruction level as the fraction of sites occupied. In the hypothesis of obstructions produced by displaced atoms, the obstruction level is the fraction of displaced atoms multiplied by 1.5, because there are 1.5 more atoms than interstitial sites S1 and S1'. Therefore, the considered set of obstruction levels corresponds respectively to 0.7, 3.3, 7, 13% of displaced atoms. Table 4 provides all obtained diffusion coefficients (*Ea* and D_0) along the *a*/*b*-axis and *c*-axis and associated closure temperatures

Along *a*- and *b*-channels the diffusion coefficient ($D_{a,b}$ or $D_{x,y}$) is only slightly affected by the amount of obstruction (Figure 7A). The curves do not diverge significantly from each other; at most the 20% case reduces the diffusivity slightly, keeping the same slope defined by the barrier of 0.66 eV. Along the *c*-channel, obstruction strongly affects diffusivity (D_c or D_z), especially at low temperature where the slope of the diffusion behavior changes significantly (Figure 7B). An important result is that, surprisingly, the impact of obstruction on 3D diffusion is higher at low temperature with an important deviation from the ideal lattice. As the fraction of obstruction increases the dependence moves closer to the *a*/*b* diffusivity. For T<300°C all the curves are almost straight lines parallel to the *a*/*b* Arrhenius law, implying similar activation energy, but with D_0 scaling down as the level of obstruction increases.

As soon as the latter exceeds 1%, He diffusion along the *c*-axis is significantly blocked leading to a change in diffusivity. One particular outcome is that the anisotropy, which was

very strong in the ideal lattice, is reduced by a factor depending of the level of obstruction, but almost independent of the temperature. For example, at 10% obstruction the anisotropy drops down to 20. It is worth noting that the above key trends are observed experimentally by Guenthner et al. (2013), who show that He activation energy orthogonal to *c* is only slightly affected by damage, whereas with increasing damage diffusion along *c* approaches a constant *Ea* close to that of the transverse direction. This experimental effect is reproduced by our calculation. It reduces the anisotropy, compared to ideal crystal, and cannot be explained by a trapping effect alone. However, our modeled activation energy in any direction remains much smaller (64 kJ/mol) in comparison to those measured in natural zircon (Reiners et al., 2004; Guenthner et al., 2013), which are around 169 kJ/mol.

In conclusion, although obstruction strongly slows down He diffusion along *c*, it is not the primary parameter that drives retentivity of He in natural zircons. However, obstruction is the main parameter acting on the anisotropy of diffusion, reducing it strongly with respect to the ideal lattice case.

For Ne the change of diffusivity with obstruction is not progressive but total. At obstruction levels as low as 1%, Ne diffusion is already frozen because the activation energy along the *a*- and *b*-axes is so high (147 kJ/mol, Table 3). Nevertheless, as with He, diffusion pathway obstruction alone cannot reproduce the inferred natural Ne diffusion behavior of zircon; as described in section 4.2, an activation energy >180 kJ/mol is necessary to reproduce Ne ages (Gautheron et al., 2006), well above the maximum activation energy of ~147 kJ/mol obtainable from obstruction. Thus, for He and Ne, pathway obstruction mechanisms are not sufficient to block He and Ne diffusion in zircon to the degree observed in natural specimens.

4.4. Impact of traps on He and Ne diffusion in zircon

In this section, the trapping model is tested and the amount of trapping energy necessary to reproduce the inferred natural He and Ne diffusion coefficients is discussed. For this purpose,

the model published in Gerin et al. (2017) is used where the diffusion coefficient modified by damage, denoted $\widetilde{D}$, follows a formula (eq. 12) that includes a trapping term:

$$\tilde{D}(x,t) = \frac{D(T)}{\left[1 + f \times \exp\left(\frac{\Delta E_{aT}}{RT}\right)\right]} \quad \text{(Eq. 12)}$$

Where *D(T)* is the diffusion coefficient of undamaged zircon (data from this study), *f* is the damage fraction ranging from 0 to 1, representing the normalized amount of displaced atoms in the structure, and ΔE_{aT} is the additional activation energy necessary for an He or Ne atom to jump out of the trap to the next insertion site. Appendix B provides a complete explanation and demonstration of the equation, and the conversion between damage fraction and alpha dose. In this study, the trapping model is correct only if damage stays as an isolated trap and does not form a percolating network connecting to the grain surface, as then it would not be a trap anymore.

The evolution of the simulated He closure temperature using Eq. 12 to account for equivalent alpha dose is reported in Figure 8A, for a 60-µm radius spherical grain. The simulation was done for ΔE_a values of 40, 80, 120 and 140 kJ/mol, where 140 kJ/mol is the maximum predicted value from the insertion energy (ΔE_{aT}) (see section 4.2). One can observe from Figure 8A that a minimum ΔE_a of 120 kJ/mol is necessary to reproduce retentive behavior in low-damage zircon of Guenthner et al. (2013). Interestingly, the activation energies and closure temperatures reported in Figure 8B are similar to those reported for natural samples in Figure 5B, lending support to the idea that our calculations have reproduced the natural range of trap diffusivities quite accurately. For Ne, a similar simulation was done for the same 60-µm radius zircon, and results are reported in Figure 8C and D for ΔE_a of 160, 200 and 300 kJ/mol, as these values bracket the needed trapping to reproduce the inferred Ne closure temperature. One can note that a trapping energy of ≥200 kJ/mol is necessary to reproduce the inferred Ne closure temperature. The data from van Soest et al. (2013) could not be used in this figure as

562 the required information are not given in the conference paper. However, we note that the sum
563 of the insertion and migration energies we calculated for Ne corresponds to 320 kJ/mol, which
564 is comparable with the van Soest et al. (2013) value, and compatible with their Tc range if D_0
565 is adjusted.

566 For He, closure temperature will increase with the equivalent alpha-dose for relatively
567 low trapping energy ΔEa (<40 kJ/mol). It seems paradoxical that the closure temperature
568 depends only slightly on the damage fraction, as illustrated in Figure 8A, but this is well
569 understood as this fraction shows up in the pre-exponential factor f in Eq. 12, whereas the
570 activation energy is in the exponential, giving rise to a much stronger effect. In other words
571 when the trapping energy is high most of the helium is trapped, whatever the number of traps
572 provided it is higher than the number of helium atoms, and only a high temperature (some
573 hundreds of °C during geological time) can extract them from the traps. This effect has been
574 seen with the DFT calculation in zircon (Saadoune and De Leeuw, 2009) and apatite (Gerin et
575 al., 2017), yet the damage topology between the two minerals is different. However, in the case
576 of zircon a higher trapping energy is needed to reproduce experimental data with respect to
577 expectations and calculations for apatite (~30-40 kJ/mol for apatite (Gerin et al., 2017; Shuster
578 and Farley, 2009) compared to 120-140 kJ/mol for zircon). The difference can be explained by
579 the higher insertion energy for He and even higher for Ne (Table 1) in zircon compared to
580 apatite (~0.6 to 1 eV; Djimbi et al., 2015), as modification of the crystal structure during damage
581 creation will produce a site more energetically favorable compared to the lattice. In this case,
582 the insertion energy strongly drops, leading to an increase of the trapping energy until a
583 threshold ΔE_{aT}. The higher necessary trapping energy can be explained by the damage topology
584 in zircon, as the crystal structure behaves quite differently than apatite. It is well known that
585 natural apatites are almost always crystalline in contrast to zircon, which is often reported to be

partially or fully metamict (e.g. Ewing et al., 2003); additional infomation on damage can be found in Appendix B.

4.5. Damage percolation threshold

For zircon, at high dose, several authors have reported that damage overlap or percolation may create amorphous zones (e.g. Ewing et al., 2003; Pidgeon, 2014; Salje et al., 1999). The more recent amorphous-crystal threshold has been estimated to be at ~2.2×10^{18} α/g (Pidgeon, 2014), which has been interepreted as the recoil percolation damage threshold (Trachenko et al., 2003). The transition to rapidly rising diffusivity occurs at ~2×10^{18} α/g in the diffusivity data set used by Guenthner et al. (2013), although data by Anderson et al. (2017) suggest a lower value at 2-5$\times10^{17}$ α/g. In addition, Ketcham et al. (2013) calculated that alpha recoil and fission damage percolate at different thresholds than previously assumed (~2×10^{16} and ~2×10^{17} α/g for alpha-recoil damage in 6-8-step decay chains and isolated decays (no-chain) respectively, and ~2×10^{18} α/g for fission tracks), due to the elongate nature of recoil and fission damage not taken into account by Trachenko et al. (2003).

Recent ZHe data measured in Hercynian granites from the Pyrenees (Bosch et al., 2016; Vacherat et al., 2016) exhibit age versus maximum alpha dose correlations that suggest that this retentivity maximum may be reached at ~2-5$\times10^{17}$ α/g (Figure 9). It is not straightforward to estimate the effective alpha dose needed to explain an age-eU pattern, so we have provided two solutions. First, as an end-member over-estimate, we simply retain all damage for each grain throughout its entire history since crystallization at 305 Ma (U/Pb age); the dose can be no higher than this (Figure 9A). Second, we posit that the divergence of measured ages was due to a reheating and partial resetting event at some time in the past that caused more He loss in the less retentive grains, and so we should consider only the possible damage production prior to that event. A conservative estimate for its timing is the age of the youngest grain, leading to the

relationship shown in Figure 9B. Even this dose is likely to be a significant over-estimate of the pertinent dose for explaining the spread in ages, as it presumes that after crystallization damage retention began immediately.

The implied transition dose from increasing to decreasing He retentivity is significantly lower than to the one considered in the RDAAM model of Guenthner et al. (2013) and is closer to the no-chain alpha recoil percolation level calculated by Ketcham et al. (2013). The no-chain case is a possibly more appropriate approximation for connectivity that leads to fast pathways, as the connectivity due to U and Th decay chains is "tip to tip", and thus dominated by potentially obstructed regions at the boundaries of tracks. The dose range over which the non-chain percolating network expands to encompass the majority of recoil damage roughly coincides with the negative dose-age correlation in the Pyrenean samples, in the range 2 to 5×10^{17} α/g, significantly below the dose range where the Guenthner et al. (2013) model postulates a fall in retentivity (above ~2×10^{18} α/g). Such a lower alpha dose threshold for percolation can also explain why samples in old and stable crustal blocks (Reiners et al., 2005) often displays only negative correlations between ZHe and eU (a proxy used for the alpha dose). In such cases the maximum potential retentivity that connects negative and positive correlations could not be documented because it would correspond to very low and atypical U concentrations for zircon.

We infer from the Pyrenean samples that the recoil damage threshold will be at a value ranging around ~2-5×10^{17} α/g, as already proposed by Anderson et al. (2017), far below the ~2×10^{18} α/g proposed by Guenthner et al. (2013).

4.6. Implication for zircon (U-Th)/He and (U-Th)/Ne thermochronometry

He and Ne diffusion coefficients in 3D obtained in this study and the investigation of mechanisms that can modify He and Ne diffusivity demonstrate that obstruction and trapping alter diffusivity significantly (Figure 10). Based on atomic investigation of He diffusion

energetics, we can predict how He will diffuse in the zircon structure. Figure 10A provides a schematic illustration of a diffusion pathway as postulated by our work. The He atom will diffuse primarily along the *c*-axis following a random diffusion pathway. He diffusion is facilitated along the *c*-axis because of the low migration energy; obstruction could slightly change the trajectory but the He atom can diffuse easily along the *a*-axis to get around any obstructed pathway. Following the example pathway of Figure 10A, the He atom is trapped in a large defect (i.e. recoil damage, voids, fluid inclusion), with a very low insertion energy (potentially approaching 0). The He atom will need a maximum activation energy of 1.7 eV (<164 kJ/mol) to go back to the crystal lattice (Fig. 10A). After that He diffuses again easily in the lattice from site to site along the a-axis and *c*-axis (passage through the rhombic gap is insignificant due to high migration energy, Fig. 4), until it reaches a second large energy well. In this case the damage is connected to other damage extending to the crystal surface (Fig. 10A). In terms of energy, we can infer from our model that in the connected area, because the lattice is distorted, the migration energy may be lowered. He insertion energy is thus very low and the He atom will diffuse in the connected damage zone with lower energy barriers. In Figure 10A, we predict that the He migration in the damage ranges from 1.4 to 0.9 eV (135 to 87 kJ/mol). Indeed, several geological studies show that for high damage dose, ZHe ages are similar to AFT ages (see Fig. 9 for the Pyrenean case example), and in some cases are even younger or equivalent to AHe ages (Johnson et al., 2017). This implies that at high dose (>10^{18} α/g), He retentivity is low in damage zone, with Tc of 110 to 50°C and thus *Ea* of 135 to 90 kJ/mol. We thus anticipate that, as opposed to the harmonic averaging model by Guenthner et al. (2013), diffusivity in zircon after the percolation transition may be controlled by the energetics and topology of the damage network.

Figure 10B combines our modeling of trapping and obstruction with natural data in terms of the closure temperature evolution as a function of the alpha dose. First, obstruction of

diffusion pathways reduces diffusivity, not as efficiently as trapping but possibly enough to play a role in addition to it. Indeed, at sufficient obstruction levels (> 20% for He and 1% for Ne), diffusion for He and Ne will be only possible when it includes a component of motion along the *a*- and *b*-axis (Table 3). The resulting diffusion behavior will still not be retentive enough to reproduce natural data, however. He and Ne global activation energy *Ea* values are respectively 63 kJ/mol and 147 kJ/mol, while values of 120-140 kJ/mol and >180 kJ/mol are needed (Figure 10B for He). The 20% obstruction level corresponds to 13% of atoms displaced (and so to an equivalent dose of ~10^{18} α/g) as explained in Appendix B, and corresponds to an equivalent closure temperature of approximately -75°C assuming a D_0 of 1.5×10^{-7} m^2/s. This value is not very tightly constrained, but provides a reasonable, illustrative first estimate of He retention.

If our modeling is correct, it is possible to make some predictions. First, for He and Ne, a quite high trapping energy is necessary to reproduce closure temperatures inferred from natural samples (Figure 8 and Figure 10B), and we predict maximum possible trapping energies with ΔEa_T of 140 kJ/mol (E_{mig}=1.46 eV) and 300 kJ/mol (E_{mig}=3.10 eV) for He and Ne respectively. These trapping energies (ΔEa_T) are within the limits provided by our DFT calculations, as discussed in section 4.2. It means that the total energy needed to go back in the crystal structure will be 164 kJ/mol ($E_{insertion}$ + E_{mig}=1.7 eV) and 320 kJ/mol ($E_{insertion}$ + E_{mig}=3.32 eV) for He and Ne respectively. Second, based on published very young volcanic zircon of ZHe ages coherent with other methods (e.g. Farley et al., 2002), we can infer that for low alpha dose (~1-2x10^{15} α/g), He is retentive to surface temperature implying a Tc of ~60-100°C (Fig. 10B). Between low damage and the threshold, we could anticipate that Tc may increase following a non-linear (i.e. cubic or exponential) law as is the case for apatite (Flowers et al., 2009), as ΔEa increases until the ΔEa_T threshold (Fig. 10B). As damage fraction increases, clustering increases also and damaged domains with different sizes will form. In this

case, the trapping energy can increase as proposed by Recanati et al. (2017) for apatite. It is interesting to note that the highest closure temperatures obtained by Guenthner et al. (2013) can be explained by increasing trapping energy when damage dose increases up to a maximum (Fig. 8A). For Ne, the maximum activation energy predicted in this study is similarly very close to the one reported by van Soest et al. (2013), and we can anticipate a complex relationship of Ne diffusion with damage dose similar to He.

After some damage threshold, He diffusion increases (Tc decreases), although the Pyrenees samples (Bosch et al., 2016; Vacherat et al., 2016) and work of Johnson et al. (2017) indicate that the threshold dose may be lower than indicated by Guenthner et al. (2013). The source of this discrepancy may be a complex function of damage accumulation and annealing, and more work on this issue is essential. For example, Ginster et al. (2018) document a complicated relationship between damage dose and annealing rate, implying a very complex system.

The other implication for a maximum of retentivity located in the vicinity of the no-chain alpha damage percolation level (Fig. 9) would be that the dependence of closure temperature on damage fraction increase can be significantly steeper than modeled with Eq. 12 (Fig. 10B) if a single ΔEa_T value is assumed. This additional level of complexity will also have implications for developing very precise future quantitative models to predict individual T_C values for single zircon grains. Such a potential scenario supported by natural data will require new experimental diffusion data to document carefully this key window of alpha-dose in the range of the no-chain percolation level.

5. Conclusions

In this contribution, we have used a series of computational and theoretical tools to provide a mechanistic view of the manner in which He and Ne diffuse in zircon. In particular, we have characterized the undamaged crystalline state and its energy structure at the atomic

scale with respect to the diffusing atoms, and how trapping and obstruction as may result from damage or inherent defects affect retention at the grain scale. The set of insights gained can help leverage ongoing analytical efforts to unravel the complex behavior of the (U-Th)/He and (U-Th)/Ne systems in natural settings.

Using Density Functional Theory and Transition State theory, we have calculated the insertion energies for He and Ne in ideal zircon, as well as the migration pathways along the *a/b* and *c* axes and the migration energies for each jump. For diffusion in the *a/b* direction, we document the energetics of the rectangular and rhombic pathways to neighboring interstitial sites. Our insertion energies for He are similar to previous work, but our migration energies and their interrelationships are different; notably, our work finds that the relative migration energies along the *c*-axis channel and through the rectangular and rhombic *a/b* gaps are approximately 0.24 vs. 0.66 and 2.60 eV for He, and 0.22 vs. 1.53 eV and infinite for Ne. One important finding is that our insertion energies, in combination with our migration energies, predict the maximum activation energies possible for the zircon He and Ne systems, which are consistent with literature values.

Our results corroborate previous theoretical and analytical work implying that pristine zircon is non-retentive for He due to low migration energies along the *c*-axis channels in the crystal structure. We also obtain the unexpected result that Ne moves even more freely than He through an unblocked *c*-axis channel, due to the distortion it causes in the insertion site. Both systems therefore require additional factors to explain their natural behavior. Using the Kinetic Monte Carlo method we show that obstruction of *c*-axis pathways forces the migration energetics to become more similar to the slower *a/b* direction as blockages increase, causing diffusion to become effectively isotropic on the grain scale and characterized by rectangular-path-jump energetics. This effect is insufficient to explain slow diffusion of He in zircon, but has a larger impact on Ne, as rectangular *a/b* transitions are much higher-energy, and rhombic

735 ones are impassable. Of the mechanisms we inspect, we find that trapping is required to explain
736 the high retention of He and Ne observed in natural zircon.
737 We consider the topology of radiation damage in the context of a data set from Pyrenees
738 granites that indicates a transition from falling to rising diffusivity at a much smaller dose than
739 posed in the Guenthner et al. (2013) diffusivity model, closer to ~2-5×10^{17} than 2×10^{18} α/g.
740 The transition dose may correspond to the no-chain alpha recoil percolation threshold of
741 Ketcham et al. (2013), suggesting that tip-to-tip recoil track connectivity is not sufficient to
742 form fast diffusion pathways, but more interpenetrative damage intersections can. Increasing
743 track intersections may also create more and deeper traps, and the evolution of not just trap
744 abundance but also trap energetics may be necessary to arrive at a quantitative understanding
745 of rare gas diffusion in natural zircon.

746 **Acknowledgment**

747 This project and salary for Duval Mbongo-Djimbi were funded by the Agence National
748 de la Recherche – grant no. ANR-12-BS06-0005-01. DIM OXYMORE funded by the region
749 île de France is thanked for salary for Hilal Balout. We thank Christophe Diarra for his precious
750 help in managing the IPNO cluster GRIF (http:// www.grif.fr). William Guenthner is warmly
751 thanked for sharing the diffusion data of his 2013 contribution. Daniele Cherniak, Peter Reiners
752 and Martin Danišík are warmly thanked for their constructive reviews.

753 **Appendix A and B - Supplementary data**

754 Supplementary data associated with this article can be found, in the online version.

References

Anderson A.J., Hodges K.V. and van Soest M.C. (2017) Empirical constraints on the effects of radiation damage on helium diffusion in zircon. *Geochim. Cosmoch. Acta*. **218**, 308-322.

Balout H., Roques J., Gautheron C., Tassan-Got L. and Mbongo-Djimbi D. (2017a) Helium diffusion in pure hematite (α-Fe_2O_3) for thermochronometric applications: a theoretical multi-scale study. *Computational and Theoritical Chemistry*, **1099**, 21-28.

Balout H., Roques J., Gautheron C. and Tassan-Got, L. (2017b) Computational investigation of the interstitial neon diffusion in pure hematite, α-Fe_2O_3. *Computational Materials Science*, **128**, 67-74.

Bengtson A., Ewing R.C. and Becker U. (2012) He diffusion and closure temperatures in apatite and zircon: A density functional theory investigation. *Geochim. Cosmoch. Acta*, **86**, 228-238.

Bortz A.B., Kalos M.H. and Lebowitz J.L. (1975) A new algorithm for Monte Carlo simulation of Ising spin systems. *J. Comput. Phys.*, **17**, 10-18.

Bosch V., Teixell G.A., Jolivet M., Labaume P., Stockli D., Domènech M. and Monié P. (2016) Timing of Eocene–Miocene thrust activity in the Western Axial Zone and Chaînons Béarnais (west-central Pyrenees) revealed by multi-method thermochronology. *Comptes Rendus Geoscience*, **348**, 246–256.

Cherniak D.J., Watson E.B. and Thomas J.B. (2009) Diffusion of helium in zircon and apatite. *Chem. Geol.*, **268**, 155-166.

Danišík, M., McInnes, B.I.A., Kirkland, C.L., McDonald, B.J., Evans, J.P. and Becker, T. (2017) Seeing is believing: Visualization of He distribution in zircon and implications for thermal history reconstruction on single crystals. *Sci. Adv.* **3**. e1601121

779 Djimbi D.M., Gautheron C., Roques J., Tassan-Got L., Gerin C. and Simoni E. (2015) Impact
780 of apatite chemical composition on (U-Th)/He thermochronometry: an atomistic point
781 of view. *Geochim. Cosmoch. Acta*, **167**, 162-176.
782 Dodson M.H. (1973) Closure temperature in cooling geochronological and petrological
783 systems. *Contrib. Min. Petrol.*, **40**, 259-274.
784 Elber R. and Karplus M. (1987) A method for determining reaction paths in large molecules:
785 Application to myoglobin. *Chem. Phys. Lett.* **139**, 375-380.
786 Ewing R.C., Meldrum A., Wang L.M., Weber W.J. and Corrales L.R. (2003). Radiation damage
787 in zircon. In: Hanchar, J.M., Hoskin, P.W.O. (Ed.), Zircon. *Mineralogical Society of*
788 *America*, pp. 387–425.
789 Farley, K.A. (2000) Helium diffusion from apatite: general behavior as illustrated by Durango
790 fluorapatite. *J. Geophys. Res.* **105**, 2903-2914.
791 Farley K.A. (2007) He diffusion systematics in minerals: Evidence from synthetic monazite
792 and zircon structure phosphates. *Geochim. Cosmoch. Acta*. **71**, 4015-4024.
793 Farley K.A. and Flowers R. (2012) (U-Th)/Ne and multidomain (U-Th)/He systematics of a
794 hydrothermal hematite from Eastern Grand Canyon. *Earth Planet. Sci. Lett.*, **359-360**,
795 131-140.
796 Farley K.A. and Stockli D.F. (2002) (U-Th)/He Dating of Phosphates: Apatite, Monazite, and
797 Xenotime., *Reviews in Mineralogy and Geochemistry*, pp. 559-577.
798 Flowers R., Ketcham R.A., Shuster D. and Farley K.A. (2009) Apatite (U-Th)/He
799 thermochronology using a radiation damage accumulation and annealing model.
800 *Geochim. Cosmochim. Acta* **73**, 2347-2365.
801 Gautheron C. and Tassan-Got L. (2010) A Monte Carlo approach of diffusion applied to noble
802 gas/helium thermochronology. *Chem. Geol*. **273**, 212-224.

Gautheron C., Tassan-Got L. and Farley K.A. (2006) (U-Th)/Ne chronometry. *Earth Planet. Sci. Lett.* **243**, 520-535.

Gautheron C., Tassan-Got L., Ketcham R.A. and Dobson K.J. (2012) Accounting for long alpha-particle stopping distances in (U-Th-Sm)/He geochronology: 3D modeling of diffusion, zoning, implantation, and abrasion. *Geochim. Cosmochim. Acta* **96**, 44-56.

Gautheron C.E., Tassan-Got L., Barbarand J. and Pagel M. (2009) Effect of alpha-damage annealing on apatite (U-Th)/He thermochronology. *Chem. Geol*. **266**, 166-179.

Gerin C., Gautheron C., Oliviero E., Bachelet C., Djimbi M.D., Seydoux-Guillaume A.M., Tassan-Got L., Sarda P., Roques J. and Garrido F. (2017) Influence of vacancy damage on He diffusion in apatite investigated at atomic to mineralogical scales. *Geochim. Cosmochim. Acta* **197**, 87-103.

Ginster, U., Reiners, P. W., Nasdala, L., and Chanmuang, C. N., 2019, Annealing kinetics of radiation damage in zircon: *Geochim. Cosmoch. Acta*. **249**, 225-246.

Guenthner W., Reiners P.W., Ketcham R., Nasdala L. and Giester G. (2013) Helium diffusion in natural zircon: radiation damage, anisotropy, and the interpretation of zircon (U-Th)/He thermochronology. *Am. J. Sci.* **313**, 145-198.

Hanchar, J. M., and van Westrenen, W., 2007, Rare Earth element behavior in zircon-melt systems. *Elements*, **3**, 37-42.

Johnson, J.E., Flowers, R.M., Baird, G.B. and Maham, K.M. (2017) "Inverted" zircon and apatite (U–Th)/He dates from the Front Range, Colorado: High-damage zircon as a low-temperature (<50°C) thermochronometer. *Earth Planet. Sci. Lett.* **466**, 80-90.

Jónsson H., Mills G. and Jacobsen K.W. (1998) Nudged Elastic Band Method for Finding Minimum Energy Paths of Transitions. *Classical and Quantum Dynamics in Condensed Phase Simulations* **385 pp**.

827 Ketcham R.A., Guenthner W.R. annd Reiners P.W. (2013) Geometric analysis of radiation
828 damage connectivity in zircon, and its implications for helium diffusion. *Am. Mineral.*
829 **98**, 350-360.
830 Kohn W. and Sham L.J. (1965) Self-Consistent Equations Including Exchange and Correlation
831 Effects. *Phys. Rev.* **140**, A1133–A1138.
832 Kresse G. and Furthmüller J. (1996) Efficient iterative schemes for ab initio total-energy
833 calculations using a plane-wave basis set. *Phys. Rev. B.* **54**, 11169.
834 Kresse G. and Hafner J. (1993) Ab initio molecular dynamics for liquid metals. *Phys. Rev. B.*
835 **47**, 558(R).
836 Mills G., Jónsson H. and Schenter G.K. (1995) Reversible work transition state theory:
837 application to dissociative adsorption of hydrogen. *Surf. Sci.* **324**, 305-337.
838 Pratt L.R. (1986) A statistical method for identifying transition states in high dimensional
839 problems. *J. Chem. Phys.* **85**, 5045-5048.
840 Recanati A., Gautheron C., Barbarand J., Missenard Y., Pinna-Jamme R., Tassan-Got L., Carter
841 A., Douville E., Bordier L., Pagel M. and Gallagher K. (2017) Helium trapping in
842 apatite damage: Insights from (U-Th-Sm)/He dating of different granitoid lithologies.
843 *Chem. Geol.* **470**, 116-131.
844 Reich M., Ewing R.C., Ehlers T. and Becker U. (2007) Low-temperature anisotropic diffusion
845 of helium in zircon: Implications for zircon (U-Th)/He thermochronometry. *Geochim.*
846 *Cosmochim. Acta* **71**, 3119-3130.
847 Reiners P.W. (2005) Zircon (U-Th)/He thermochronometry. In: Reiners, P.W., Ehlers, T.A.
848 (Eds.), Thermochronology, *Rev. Mineral. Geochem*. pp. **151-179**.
849 Reiners P.W., Brady R., Farley K.A., Fryxell J.E., Wernicke B.P. and Lux D. (2000) Helium
850 and argon thermochronology of the Gold Butte block, south Virgin Mountains, Nevada.
851 *Earth Planet. Sci. Lett.* **178**, 315-326.

852 Reiners P.W., Farley K.A. and Hiskes H.J. (2002) He diffusion and (U-Th)/He
853 thermochronology of zircon: initial results from Fish Canyon Tuff and Gold Butte.
854 *Tectonophysics* **349**, 297-308.
855 Reiners P.W., Spell T.L., Nicolescu S. and Zanetti K.A. (2004) Zircon (U–Th)/He
856 thermochronometry: He diffusion and comparison with $^{40}Ar/^{39}Ar$ dating. *Geochim.*
857 *Cosmochim. Acta* **68**, 1857-1887.
858 Saadoune I. and de Leeuw N.H. (2009) A computer simulation study of the accomodation and
859 diffusion of He in uranium- and plutonium-doped zircon ($ZrSiO_4$). *Geochim.*
860 *Cosmochim. Acta* **73**, 3880-3893.
861 Saadoune I., Purton J.A. and de Leeuw N.H. (2009) He incorporation and diffusion pathways
862 in pure and defective zircon $ZrSiO_4$: A density functional theory study. *Chem. Geol.*
863 **258**, 182-196.
864 Salje E.K.H., Chrosch J. and Ewing R.C. (1999) Is "metamictization" of zircon a phase
865 transition? *Am. Mineral*. **84**, 1107-1116.
866 Shuster D. and Farley K.A. (2009) The influence of artificial radiation damage and thermal
867 annealing on helium diffusion kinetics in apatite. *Geochim. Cosmochim. Acta* **73**, 183-
868 196.
869 Shuster D., Flowers R. and Farley K.A. (2006) The influence of natural radiation damage on
870 helium diffusion kinetics in apatite. *Earth Planet. Sci. Lett.* **249**, 148-161.
871 Shuster D., Vasconcelos P., Heim J. and Farley K.A. (2005) Weathering geochronology by (U-
872 Th)/He dating of goethite. *Geochim. Cosmochim. Acta* **69**, 659-673.
873 Trachenko K., Dove M.T. and Salje E.K. (2003) Large swelling and percolation in irradiated
874 zircon. *J. Phys. Condens. Matter* **15**, L1-L7.

Vacherat A., Mouthereau F., Pik R., Bellahsen N., Gautheron C., Bernet M., Daudet M., Balansa J., Tibari B., Pinna-Jamme R. and Radal J. (2016) Rift-to-collision transition recorded by tectono-thermal evolution of the northern Pyrenees. *Tectonics* **35**, 4.

van Soest M.C., Tripathy-Lang A., Hodge K.V. and Monteleone B.D. (2013) Neon diffusion in titanite and zircon and the utility of these minerals for (U-Th)/Ne thermochronometry. In: AGU (Editor), American Geophysical Union, Fall Meeting. AGU, San Francisco.

Vineyard G.H. (1957) Frequency factors and isotope effects in solid state rate processes. *J. Phys. Chem. Solids* **3**, 121-127.

Wert C. and Zener C. (1949) Interstitial Atomic Diffusion Coefficients. *Phys. Rev.* **76**, 1169–1175.

Zeitler P.K., Herczerg A.L., McDougall I. and Honda M. (1987) U-Th-He dating of apatite: A potential thermochronometer. *Geochim. Cosmochim. Acta* **51**, 2865-2868.

Zeitler, P.K., Enkelmann, E., Thomas, J.B., Watson, E.B., Ancuta, L.D. and Idleman, B.D. (2017) Solubility and trapping of helium in apatite. *Geochim. Cosmoch. Acta.* **209**, 1-8.

Tables captions

Table 1: Helium and neon insertion energies in zircon, hematite and apatite crystal structure.

Table 2: Migration energies in eV for both helium and neon in zircon compared with the theoretical studies of He diffusion (Bengtson et al., 2012; Reich et al., 2007; Saadoune et al., 2009). Rect. and Rhom. are for the rectangular and rhombic gap.

Table 3: Diffusion parameters for He and Ne in ideal lattice.

Table 4: Diffusion coefficients (D_0 and Ea) along *a/b* and *c* axes for different percentages of obstruction, as shown in Figure 8.

Figure captions

Figure 1: Sequence of computational tools developed and used in this study. Migration energies and attempt frequencies from DFT are used with TST to calculate activation energy *Ea* and frequency factor D_0 at the atomic level for an ideal pristine crystal. Zircon crystal results from this study are used for illustration. These results are used in a KMC code to calculate in 3D diffusion paths that accounts for the effects of obstruction and trapping. The example of diffusion in apatite is shown (Djimbi et al., 2015). At the macroscopic level, for anisotropic diffusion and to account for crystal shape, a finite geometry Monte Carlo code (Gautheron and Tassan-Got, 2010) is used to calculate the (U-Th)/He age for a determined thermal history and effective closure temperature. The example of apatite and zircon crystals are shown. Finally, all these data can serve as the basis for a damage model.

Figure 2: Representation of the zircon crystal supercell (2×2×2) showing the channels along the *c*-axis (A) and along the *a*- and *b*-axes (B). He/Ne insertion sites indicated by square and circle. Along the diffusion *c*-channel and *a*- and *b*-channel (note that the *a*- and *b*-axes are identical), the different He/Ne insertion sites S_1 and S_1' are denoted (A' and B'). Along *a*- and *b*-channels, He/Ne atoms have to pass through a rhombic (Rhom.) or rectangular (Rect.) gap. Note that along the *a*-axis the sites are only S1 type whereas along *b*-axis the sites are only S1' type.

Figure 3: Evolution of the minimal energy path (MEP) between insertion site S_1 to S_1' along the *c*-channel (A) and (A') and along *a*- and *b*- channels (B) and (B') for He and Ne respectively. Rect. and Rhom. are for the rectangular and rhombic gaps. As with Figure 2, the sites along the *a* and *b*-axes are S1 and S1' respectively.

930

931 **Figure 4:** Schematic illustration of the different diffusion pathways in zircon identified
932 with the insertion energies along the three axes (*a*, *b* and *c*). The two sites S_1 and S_1' are
933 distinguished and the example of different diffusion pathways between those sites are shown.
934

935 **Figure 5:** Correlation of the activation energy E_a with frequency factor D_0 (A) and
936 closure temperature (B) determined in 3D for He and Ne (green diamonds). Results obtained
937 on natural zircon crystal by Cherniak et al. (2009); Guenthner et al. (2013); Reiners et al. (2004)
938 for He and are reported. A minimal deduced E_a value for Ne obtained from the closure
939 temperature estimate of Gautheron et al. (2006) is reported in diagram B.
940

941 **Figure 6:** Schematic representation of mechanisms that may affect diffusivity. (A) He
942 and Ne diffusion pathway depends only on diffusion coefficients between all insertion sites.
943 Ea_c, Ea_{rhom} and Ea_{rect} refer to the activation energies along the *c*-axis and through the *a*-axis
944 rhombic and rectangular gaps. The same color codes as in Figure 4 are used for diffusion
945 through rectangular or rhombic gaps. One can note that the energy to diffuse through a rhombic
946 gap is high compare to a rectangular one, and that no diffusion can occur through impassable
947 boundaries (thick black lines). (B) Some pathways are obstructed (blue cross), and He or Ne
948 can only go around the blocked paths. Same diffusion coefficient between insertion sites is
949 taken as in A. (C) Damage represented by the open blue oval can trap atoms, as the needed
950 ΔEa_T is much higher than the activation energy between interstitial sites.
951

952 **Figure 7:** Evolution of the diffusion coefficient as a function of inverse temperature
953 along *a*/*b*-axis (A) and *c*-axis (B) for various values of obstructed pathways from 1 to 20%. As
954 a reference the diffusion coefficient evolution in 3D and for all axes, and for natural zircon

(gray line; Reiners et al., 2004; orange lines with similar dashed lines from Guenthner et al., 2013) are reported in both figures.

Figure 8: Models of helium and neon closure temperature dependence on alpha dose (A, C) and activation energy (B, D). Closure temperature evolution with dose (A, C, black lines) modeled for a 60-μm radius spherical grain, using the base level diffusion coefficients obtained in this study and equation (12) to estimate the effects of dose and trapping energy. ΔEa values of 40, 80, 100, 120 and ΔEa_T of 140 kJ/mol are modeled for He, and ΔEa values of 160, 200 and ΔEa_T of 300 kJ/mol for Ne. Diagram B and D shows the evolution of the modified activation energy as a function of the calculated closure temperature. Data obtained from this study (diamonds), on natural zircon from Guenthner et al. (2013) (red dots; Figures A, B), and data from van Soest et al. (2013) for Ne diffusion are reported for comparison. Black and gray circles same as in Figure 5.

Figure 9: ZHe age evolution as a function of the equivalent alpha-dose, for two Pyrenean massifs (Bosch et al., 2016; Vacherat et al., 2016). The values for the 6-8-chain, no-chain and fission-track percolation thresholds of Ketcham et al. (2013) are reported for comparison. Apatite fission track (AFT) and apatite (U-Th)/He (AHe) ages range from Bosch et al. (2016) and Vacherat et al. (2016) are also shown for comparison.

Figure 10: (A) Schematic representation of the energetic levels of a diffusion pathway for He; a similar representation can be made for Ne. 1.46 eV is the He insertion energy, and E_{mig} is the migration energy, that can be for He 0.24, 0.66 eV for regular lattice (24 and 66 kJ/mol respectively). In a damage zone, He insertion can be lower and the resulting trapping energy will increase and can be up to 1.46 eV, resulting in a migration energy of 1.7 eV

($E_{mig.}$=164 kJ/mol). In this model, the size of the regular insertion site (a_{IS}, black arrow) is smaller than for a damage zone (a_D, blue arrow) resulting in a different energy level. (B) Evolution of the closure temperature as a function of the alpha dose (black lines). Data from Guenthner et al. (2013) (red circles) and calculated with the DFT results (this study, red square) are reported in addition to the trapping model with trapping energies ΔEa of 100, 120 and ΔEa_T 140 kJ/mol, and the blocking pathway model at 1, 5, 10 and 20% of obstruction (details about the calculation are given in Table 4). The calculated damage thresholds from Ketcham et al. (2013) and the one inferred from Pyrenees samples (Fig. 9) are also reported. Inferred closure temperature for very young zircon (<1 Ma; Farley et al., 2002), Pyrenean samples (Bosch et al., 2016; Vacherat et al., 2016) and highly damages zircon from Johnson et al. (2017) are also shown. The relation between obstructed pathways with alpha dose is not straightforward, but we estimate the transition from rising to falling closure temperature to be in the 2-5×10^{17} α/g range.

Table 1. Insertion energies for He and Ne into interstitial sites in this and other studies.

Insertion energy	Zircon, this work	Zircon, Saadoune et al. (2009)	Hematite, Balout et al. (2017a, b)	Apatite, Djimbi et al. (2015)
He (eV)	1.46	1.45	1.51	1.15 (a,b-plan); 0.66 (c-axis)
Ne (eV)	3.10	-	3.38	-

Table 2. Migration energies (in eV) for He and Ne in zircon.

	Helium			Neon		
	***c*-channel**	***a and b*-channel**		**c-channel**	***a and b*-channel**	
		Rect.	***Rhom.***		***Rect.***	***Rhom.***
This work	0.24	0.66	2.60	0.22	1.53	none
Reich et al. (2007)	0.14	0.46	1.05	-	-	-
Saadoune et al. (2009)	0.22	0.44	2.68	-	-	-
Bengtson et al. (2012)	0.44	0.43	2.64	-	-	-

Migration energies in eV for both helium and neon in zircon compared with the theoretical studies of He diffusion (Bengtson et al., 2012; Reich et al., 2007; Saadoune et al., 2009). Rect. and Rhom. are for the rectangular and rhombic gaps.

Table 3. Diffusion parameters for He and Ne in ideal lattice.

		Saddle point	E_{mig} (eV)	E_a (kJ/mol)	ν (THz)	a (Å)
He	*a* and *b*-channel	Rect.	0.66	63.7	5.50	3.35
		Rhom.	2.6	250.9	3.44	3.35
	c-channel		0.24	23.2	7.06	1.5
Ne	*a* and *b*-channel	Rect.	1.53	147.6	3.90	3.35
		Rhom.	none	none	none	3.35
	c-channel		0.22	21.2	1.36	1.5

Table 4: Diffusion coefficients (D_0 and Ea) along *a/b* and *c* axes for different percentages of obstruction, as shown in Figure 8.

% obstruction	D_0 (*c*) (m^2/s)	Ea (*c*) (kJ/mol)	D_0 (*a/b*) (m^2/s)	Ea (*a,b*) (kJ/mol)	Tc (°C)
0	1.6×10^{-7}	23.1	1.5×10^{-7}	63.6	-193
1	4.6×10^{-4}	61.8	1.5×10^{-7}	63.6	-100
5	1.1×10^{-5}	60.6	1.5×10^{-7}	63.6	-88
10	2.3×10^{-6}	60.1	1.5×10^{-7}	63.6	-83
20	5.6×10^{-7}	61.9	1.1×10^{-7}	54.0	-73

Closure temperature calculated for a 100x100x200 µm prism, cooling rate of 10°C/Ma and no ejection.

Figure1

Density Functional Theory (DFT) / Nudge Elastic Band (NEB)

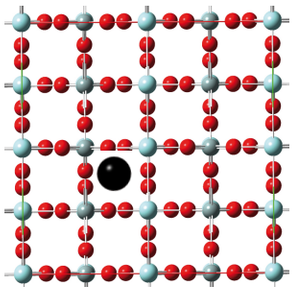

Crystal structure

Interstitial sites and insertion energy

Migration energies: E_{mig}

Eigen-frequencies: ν

DFT–output / TST–input

Transition State Theory (TST)

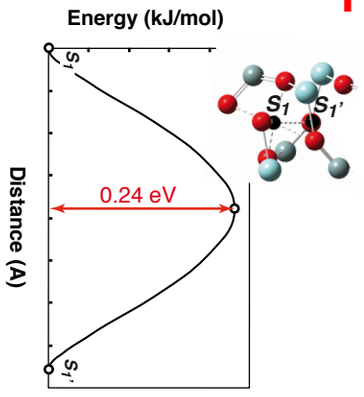

Attempt frequencies: $\nu* = f(\nu)$

Migration rates: $\Gamma=f(E_{mig},\nu*)$

D_0 (homogeneous): $D_0=f(\Gamma,a)$

TST–output / KMC–input

Kinetic Monte Carlo (KMC)

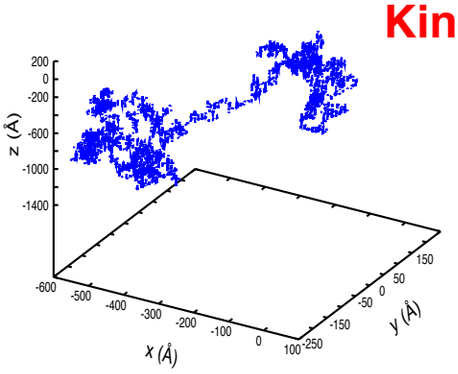

D(T) heterogeneous diffusion pathways: $f(\Gamma,a,T)$

$D(T)=D_0\exp(-E_a/k_bT)$

KMC–output / MC input

homogeneous

Finite geometry Monte Carlo (MC)

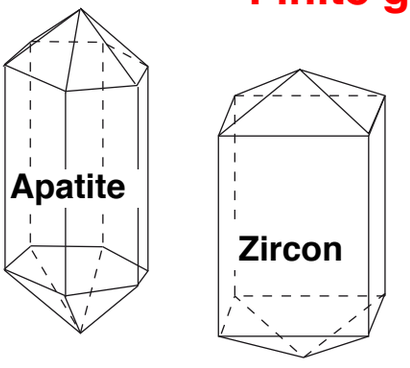

He age

Tc

MC–output / Damage model

Figure2

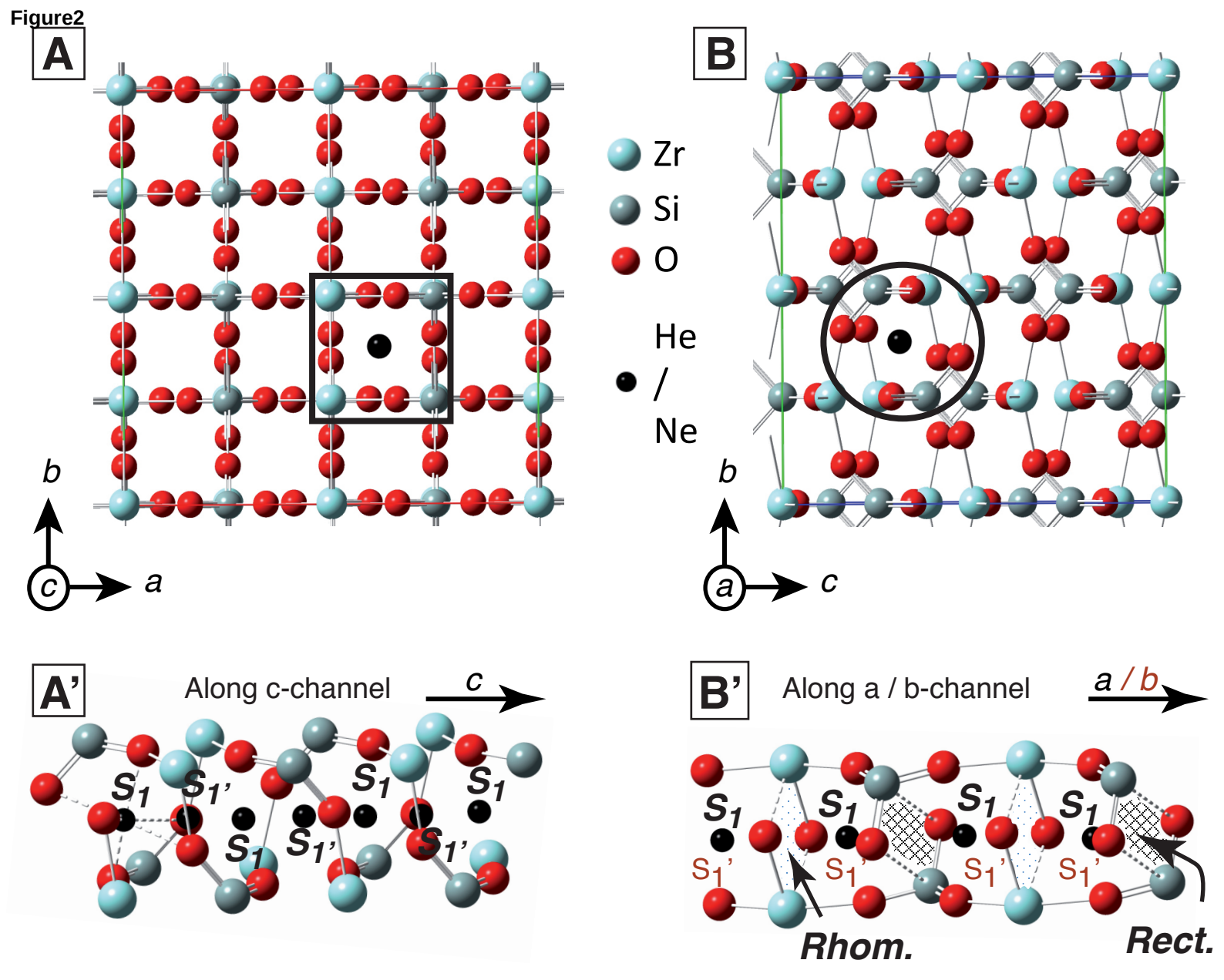
A
B
Zr
Si
O
He / Ne
b
c
a
b
a
c
A'
Along c-channel
c
S1
S1'
S1
S1'
S1
S1'
S1
S1
B'
Along a / b-channel
a / b
S1
S1'
S1
S1'
S1
S1'
S1
S1'
Rhom.
Rect.

Figure3

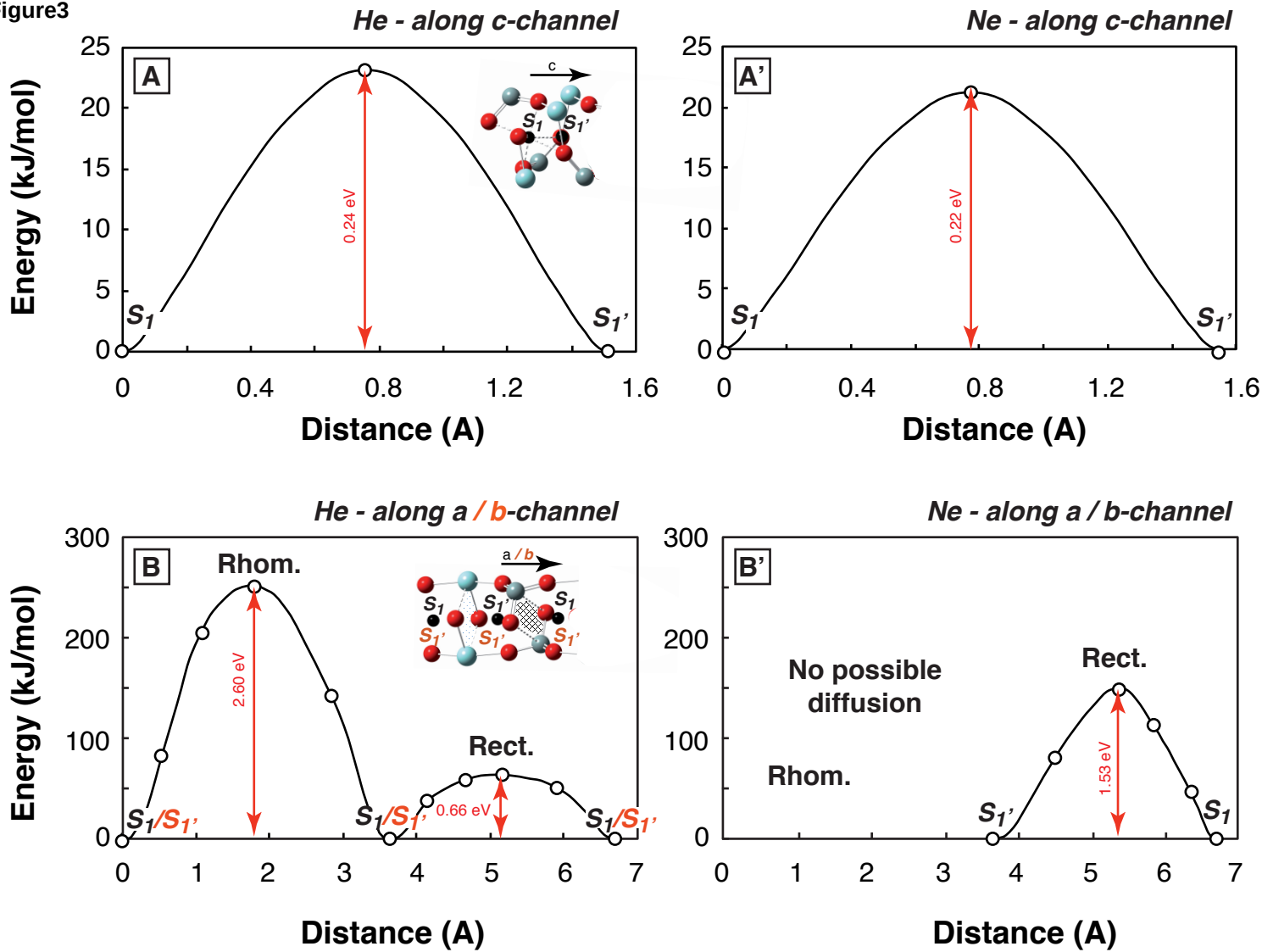
He - along c-channel
Ne - along c-channel
A
A'
c
S_1
S_1'
0.24 eV
0.22 eV
Energy (kJ/mol)
Distance (A)
He - along a / b-channel
Ne - along a / b-channel
B
B'
Rhom.
a / b
2.60 eV
Rect.
0.66 eV
S_1/S_1'
No possible
diffusion
Rhom.
Rect.
1.53 eV

Figure4

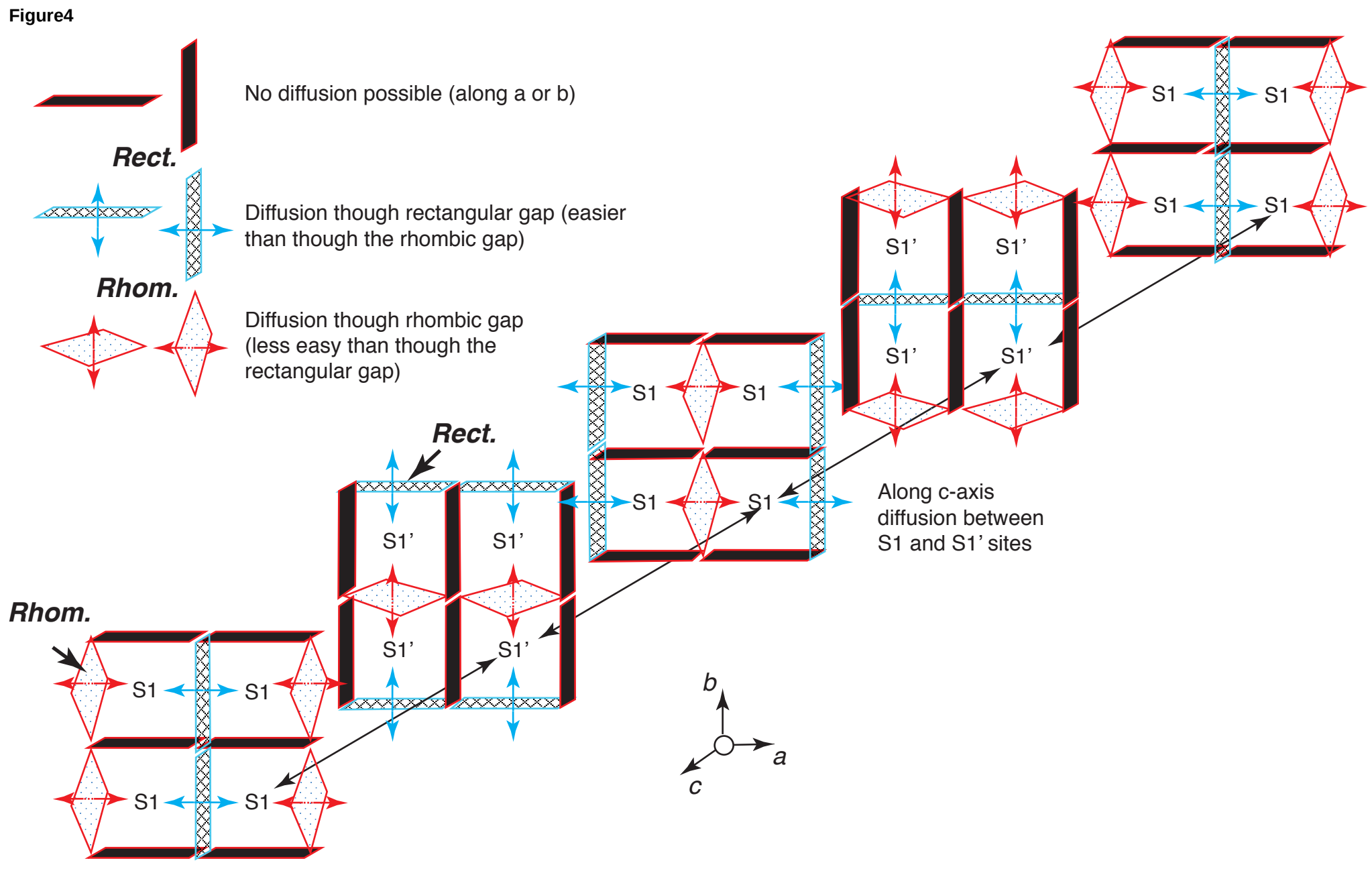
No diffusion possible (along a or b)
Rect.
Diffusion though rectangular gap (easier than though the rhombic gap)
Rhom.
Diffusion though rhombic gap (less easy than though the rectangular gap)
S1
S1'
Along c-axis diffusion between S1 and S1' sites
b
a
c

Figure5

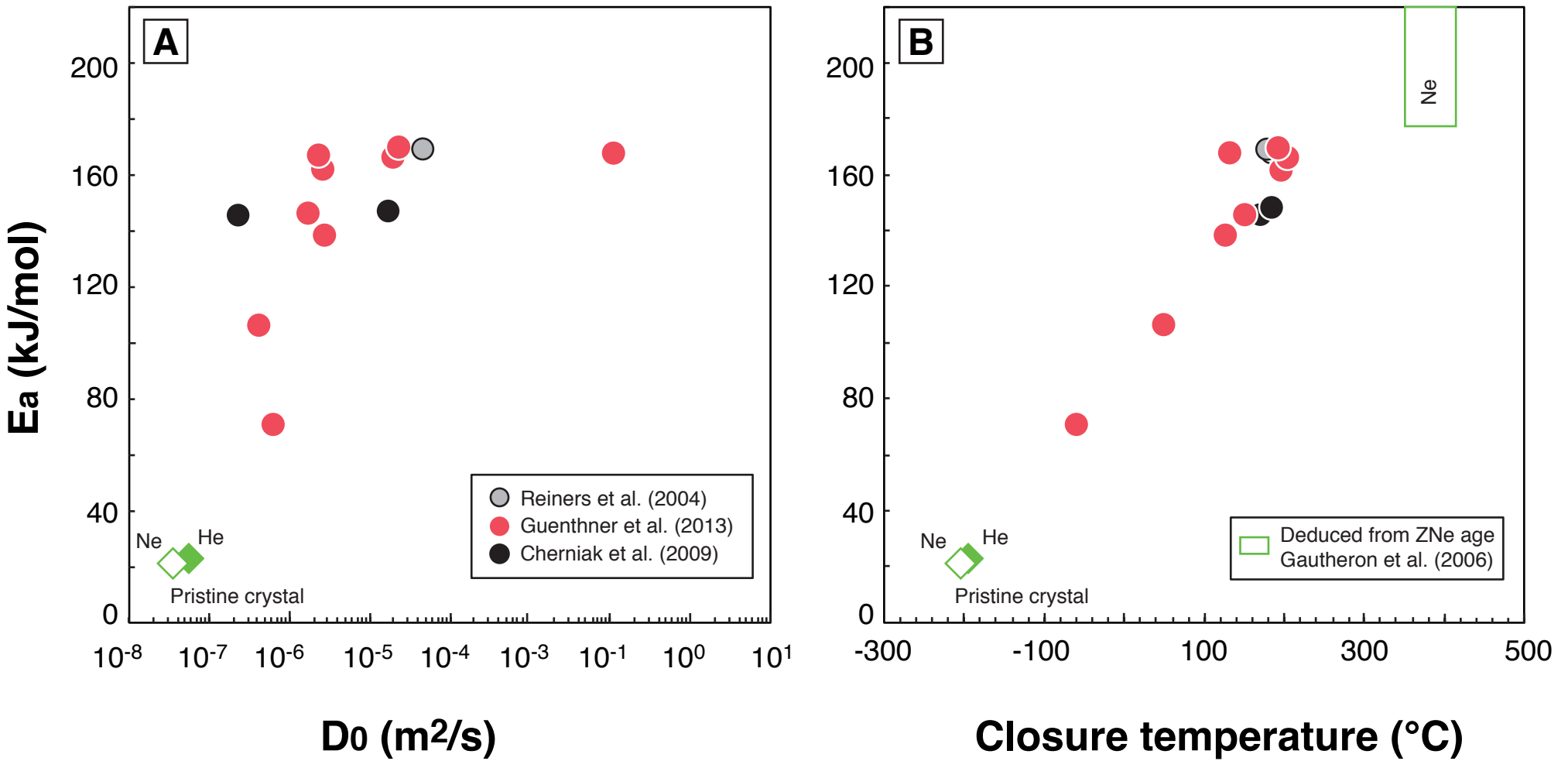
A
B
Ea (kJ/mol)
200
160
120
80
40
0
10-8
10-7
10-6
10-5
10-4
10-3
10-1
100
101
D0 (m2/s)
Reiners et al. (2004)
Guenthner et al. (2013)
Cherniak et al. (2009)
Ne
He
Pristine crystal
Ne
Deduced from ZNe age
Gautheron et al. (2006)
-300
-100
100
300
500
Closure temperature (°C)

Figure6

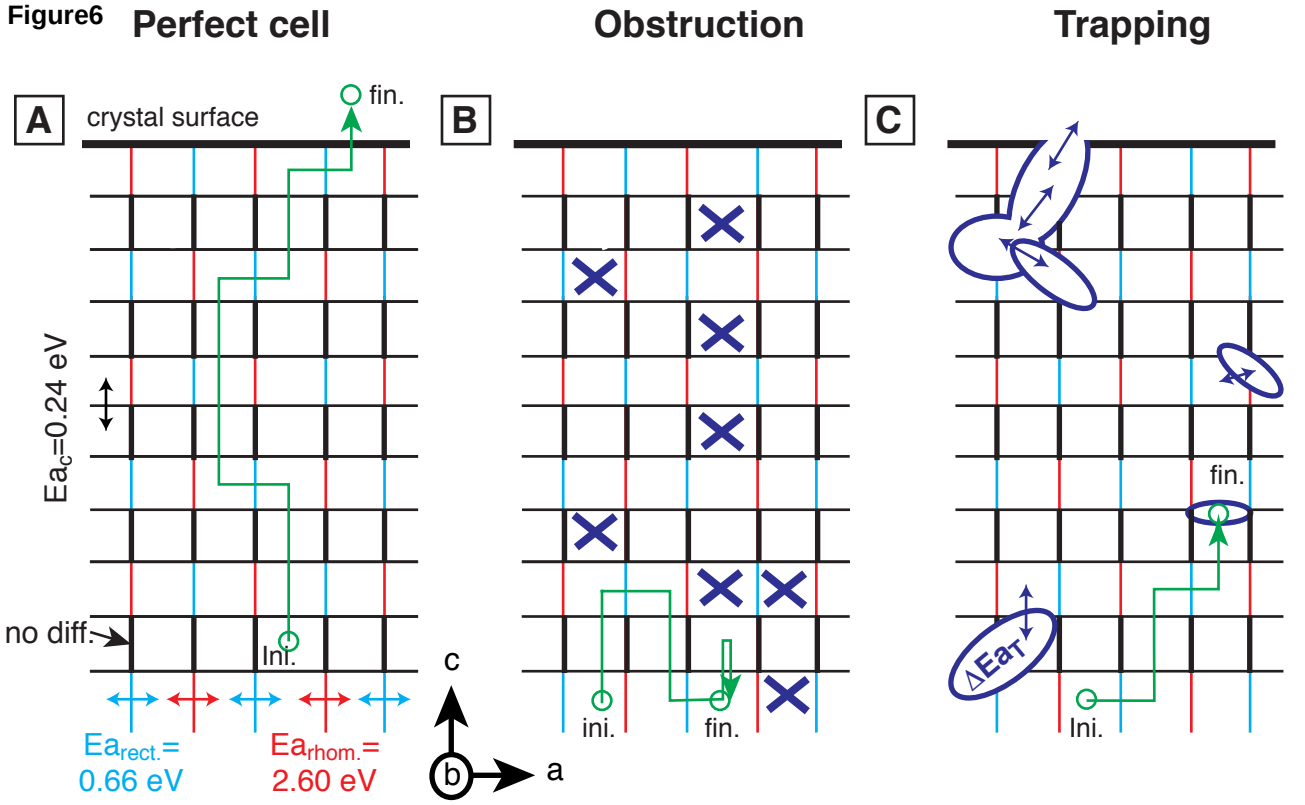
Perfect cell
Obstruction
Trapping
A
crystal surface
fin.
Eac=0.24 eV
no diff.
Ini.
Earect.=
0.66 eV
Earhom.=
2.60 eV
B
ini.
fin.
C
fin.
ΔEaT
Ini.
c
b
a

Figure7

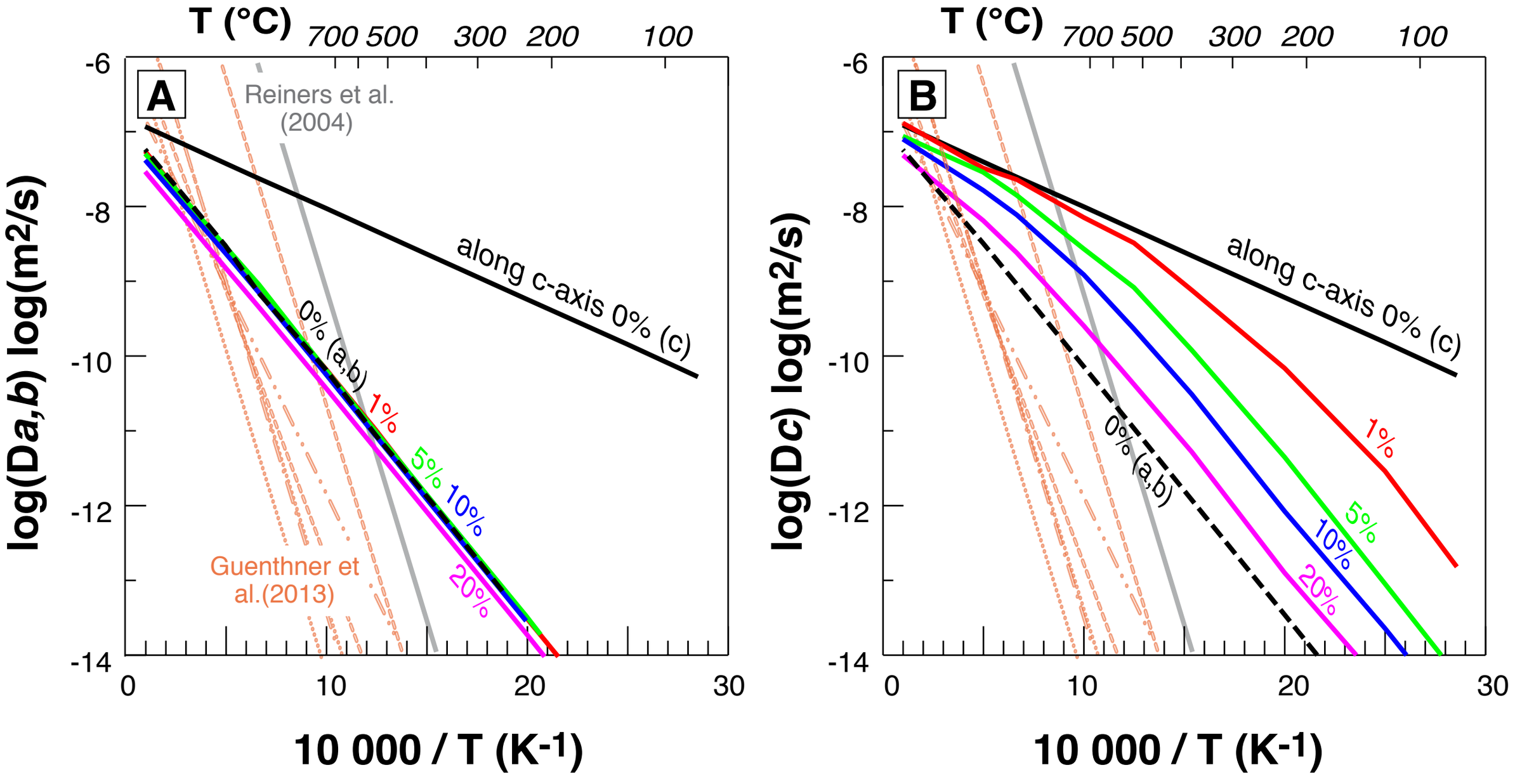
T (°C)
700 500
300
200
100
A
Reiners et al.
(2004)
along c-axis 0% (c)
0% (a,b)
1%
5%
10%
20%
Guenthner et
al.(2013)
log(Da,b) log(m2/s)
-6
-8
-10
-12
-14
0
10
20
30
10 000 / T (K-1)
B
log(Dc) log(m2/s)

Figure8

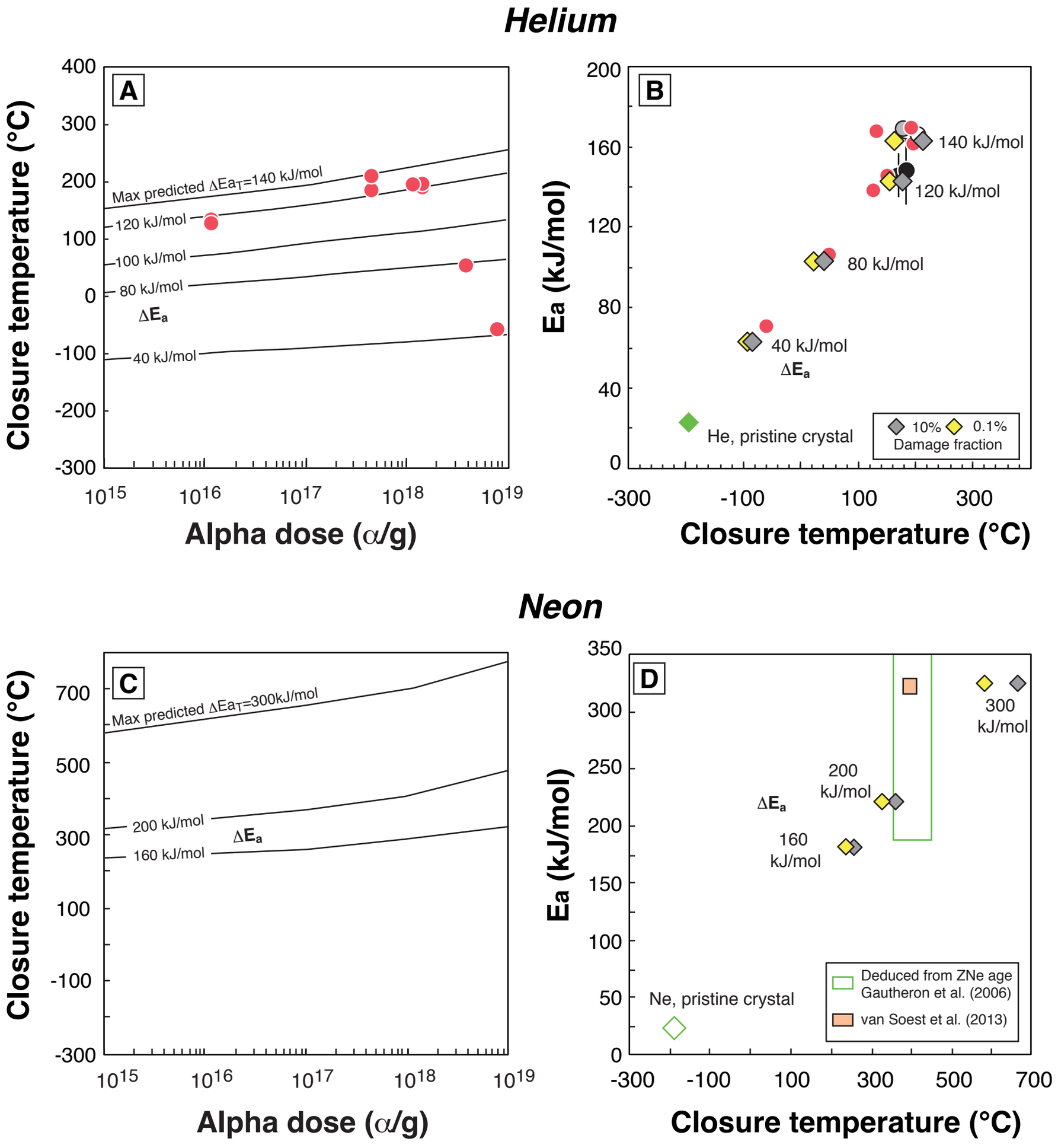
Helium
A
Max predicted ΔEa$_T$=140 kJ/mol
120 kJ/mol
100 kJ/mol
80 kJ/mol
ΔE$_a$
40 kJ/mol
Closure temperature (°C)
Alpha dose (α/g)
B
140 kJ/mol
120 kJ/mol
80 kJ/mol
40 kJ/mol
ΔE$_a$
He, pristine crystal
10%
0.1%
Damage fraction
Ea (kJ/mol)
Closure temperature (°C)
Neon
C
Max predicted ΔEa$_T$=300kJ/mol
200 kJ/mol
ΔE$_a$
160 kJ/mol
Closure temperature (°C)
Alpha dose (α/g)
D
300 kJ/mol
200 kJ/mol
ΔE$_a$
160 kJ/mol
Ne, pristine crystal
Deduced from ZNe age
Gautheron et al. (2006)
van Soest et al. (2013)
Ea (kJ/mol)
Closure temperature (°C)

Figure9

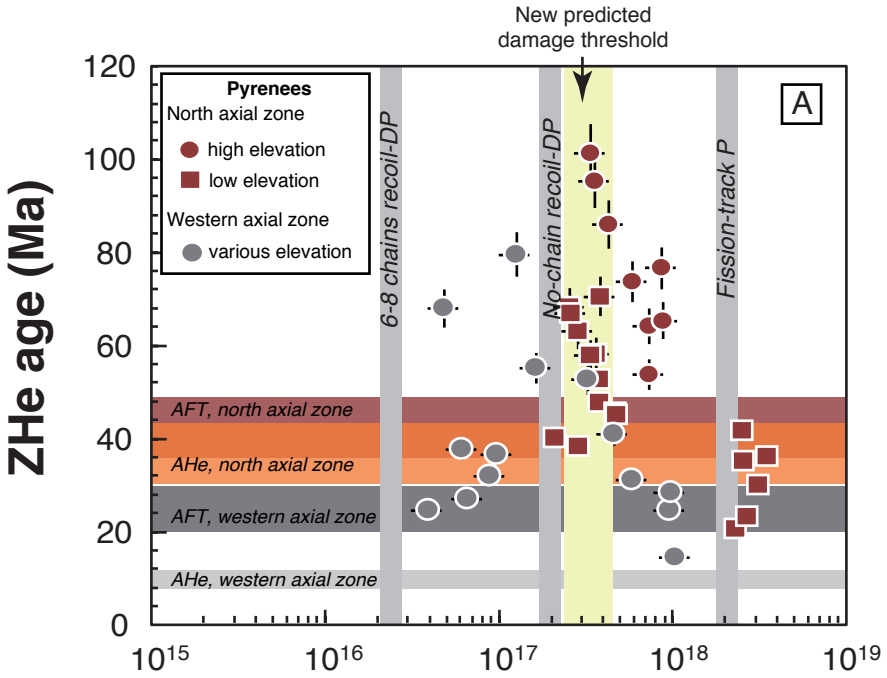
New predicted
damage threshold
A
Pyrenees
North axial zone
high elevation
low elevation
Western axial zone
various elevation
6-8 chains recoil-DP
No-chain recoil-DP
Fission-track P
AFT, north axial zone
AHe, north axial zone
AFT, western axial zone
AHe, western axial zone
ZHe age (Ma)
120
100
80
60
40
20
0
10^15
10^16
10^17
10^18
10^19
Alpha dose (α/g)
maximum possible current dose

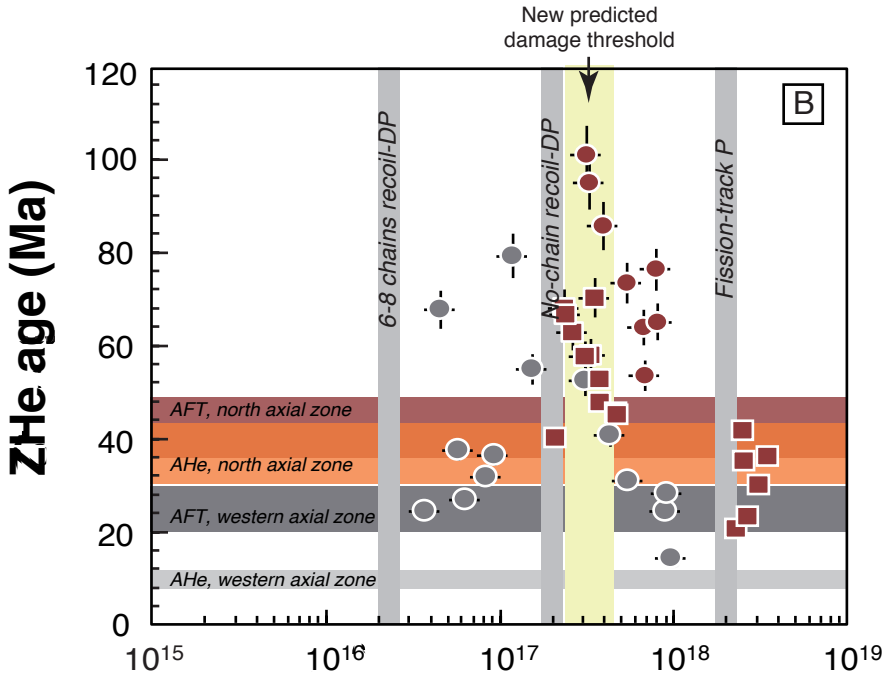
New predicted
damage threshold
B
6-8 chains recoil-DP
No-chain recoil-DP
Fission-track P
AFT, north axial zone
AHe, north axial zone
AFT, western axial zone
AHe, western axial zone
ZHe age (Ma)
120
100
80
60
40
20
0
10^15
10^16
10^17
10^18
10^19
Alpha dose (α/g)
maximum possible dose at estimated
time of partial resetting

Figure10

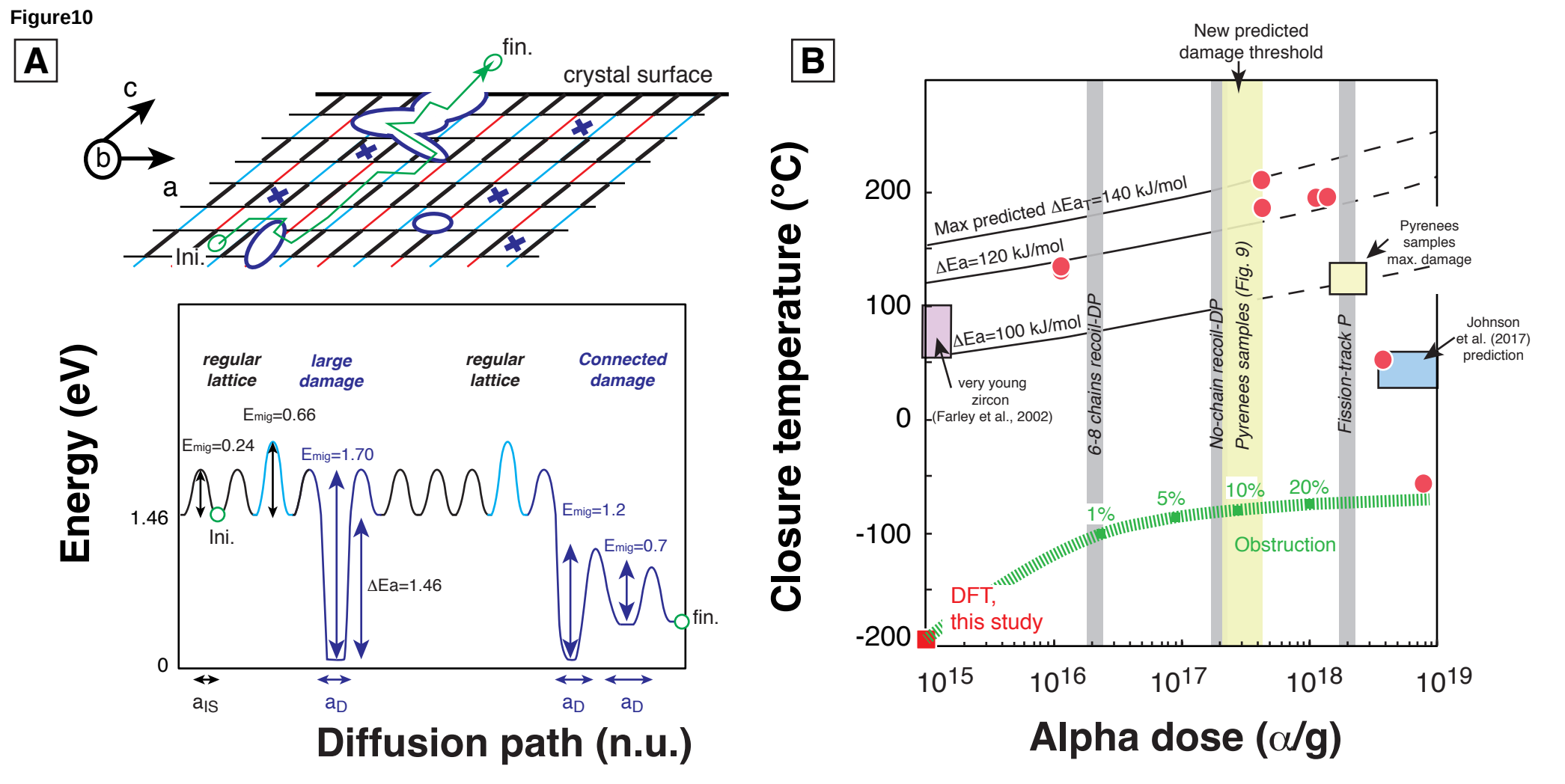
A
fin.
crystal surface
c
b
a
Ini.
regular lattice
large damage
regular lattice
Connected damage
Emig=0.66
Emig=0.24
Emig=1.70
Emig=1.2
Emig=0.7
ΔEa=1.46
Ini.
fin.
1.46
0
Energy (eV)
aIS
aD
aD
aD
Diffusion path (n.u.)
B
New predicted damage threshold
Max predicted ΔEaT=140 kJ/mol
ΔEa=120 kJ/mol
ΔEa=100 kJ/mol
Pyrenees samples max. damage
Johnson et al. (2017) prediction
very young zircon (Farley et al., 2002)
6-8 chains recoil-DP
No-chain recoil-DP
Pyrenees samples (Fig. 9)
Fission-track P
1%
5%
10%
20%
Obstruction
DFT, this study
200
100
0
-100
-200
Closure temperature (°C)
10^15
10^16
10^17
10^18
10^19
Alpha dose (α/g)

Electronic Annex

Click here to download Electronic Annex: Appendix_sept2019.docx